**ORIGINAL PAPER**

# Structural and metamorphic evolution of the southern Sanandaj-Sirjan zone, southern Iran

Parisa Gharibnejad[1,4,5] · Claudio L. Rosenberg[2] · Philippe Agard[2] · Ali Kananian[1] · Jafar Omrani[3]

## Abstract

The southern Sanandaj-Sirjan Zone (SSZ) forms the core of the Zagros orogen and consists of a stack of four major tectonic units, all of which were thrust southwestward over the Neyriz ophiolites. Precambrian and early Paleozoic rocks were affected by high-grade metamorphism, whilst the late Paleozoic (Carboniferous and Permian) and Mesozoic rocks are of low grade to unmetamorphosed. Geothermobarometric results indicate that the investigated area experienced peak temperature–pressure conditions of ~ 650 °C and 8–9 kbar, before being partly overprinted by greenschist facies conditions. We identified two main deformational phases (D2, D3) and some relics of an older one (D1) in the southern SSZ. D1 is inferred based on local evidence of tight D2 folds that fold a pre-existing schistosity (S1), associated with prograde- and peak metamorphism. D2 shows large-scale, tight-to isoclinal F2 folds and a penetrative S2 foliation, forming the dominant foliation in our study area. The P–T path is clockwise and associated with a geothermal gradient of ~ 20 °C/km, suggesting a collision-related geodynamic setting, preceding D2, and possibly linked to an early stage of D1. D3 is characterized by open folds (F3) and thrusts developed after greenschist facies metamorphism. Based on the metamorphic grade and stratigraphic age of folded units, D2 is inferred to be Eo-Cimmerian, and D3 post-Cretaceous, coeval to the Zagros orogeny. Concerning the oldest phase (D1), for which only circumstantial structural evidence exists, we discuss whether its age is pre-Cimmerian, possibly Variscan, or Eo-Cimmerian as suggested in previous literature. This study uses metamorphic assemblages and structures of the southern SSZ, to retrace its geodynamic evolution, which started with burial associated with high-temperature metamorphism, followed by Eo-Cimmerian shortening, and finally terminated with additional shortening related to the Zagros collisional event.

**Keywords** Barrovian metamorphism · Geothermobarometry · Orogenic phases · P–T path · Sanandaj-Sirjan Zone · Structural analysis

## Introduction

The Alpine–Himalayan chains, extending from the western Pacific to the eastern Mediterranean, resulted from the closure of the Neotethyan ocean and subsequent continental collision between the African–Arabian–Indian and Eurasian plates. In the central segment of the Neotethyan zone, the collision between Arabia and Eurasia resulted in the formation of the Turkish–Iranian plateau (Brunet and Cloetingh

✉ Ali Kananian
kananian@ut.ac.ir

Parisa Gharibnejad
Pa.gharibnezhad@ut.ac.ir

Claudio L. Rosenberg
claudio.rosenberg@sorbonne-universite.fr

Philippe Agard
philippe.agard@sorbonne-universite.fr

Jafar Omrani
j.omrani@gmail.com

[1] School of Geology, College of Science, University of Tehran, Tehran, Iran

[2] Sorbonne Université, CNRS-INSU, Institut des Sciences de la Terre de Paris, ISTeP UMR 7193, CNRS, 75005 Paris, France

[3] Geological Survey of Iran, Tehran, Iran

[4] National Key Laboratory of Ecological Security and Resource Utilization in arid areas, Xinjiang Institute of Ecology and Geography, Chinese Academy of Sciences, Urumqi 830011, China

[5] Research Centre for Mineral Resources, Xinjiang Institute of Ecology and Geography, Chinese Academy of Sciences, Urumqi 830011, China

2003) and of the Zagros chain, which exposes the Sanandaj-Sirjan Zone (SSZ) all along its core.

Opening of the Neotethys ocean during the late Paleozoic (~290–250 Ma; Ricou 1994; Stampfli and Borel 2002) detached a series of crustal fragments, called Cimmerian blocks, from the northern margin of Gondwana (Stöcklin 1974a; Şengör 1979; Berberian and King 1981; Boulin 1991; Golonka 2004; Mattei et al. 2015). Those fragments collided with Eurasia during the Late Triassic Cimmerian orogeny accompanying the closure of the Paleotethys (~220–210 Ma; e.g. Şengör 1987; Horton et al. 2008; Zanchi et al. 2009; Fergusson et al. 2016). The evolution of the Cimmerian blocks is poorly known, in part due to the lack of kinematic data to constrain their displacements respect to each other and to Eurasia. The northern boundary of the Cimmerian blocks, along the Paleotethys suture (Fig. 1a), runs along the present-day Alborz and Kopeh-Dagh ranges in northern and northeastern Iran and extends to northern Afghanistan (the Hindu Kush and Badakhshan), Tibet and China (e.g. Ricou 1994; Stampfli and Borel 2002; Barrier et al. 2018). The southern boundary of the Cimmerian blocks lies along the Neotethyan suture, i.e. the Main Zagros Thrust (MZT; Fig. 1a, b), which formed after the collision of these blocks with the Afro-Arabian plate. While the precise onset of the Arabia-Eurasia collision has been a matter of debate (e.g. Mohajjel et al. 2003; Golonka 2004; François et al. 2014), most authors tend to agree that continental collision started in the Oligocene (Agard et al. 2005, 2011; Ballato et al. 2008; Paul et al. 2010; Mouthereau et al. 2012; McQuarrie and Hinsbergen 2013).

Three following main blocks make up the Cimmerian crustal fragments of Iran: the Sanandaj-Sirjan Zone (SSZ), the Alborz block and the Central Iranian microcontinent (Fig. 1a). Despite being prominent features of Iranian geology, their primary location (Masoodi et al. 2013; Mattei et al. 2015; Barrier et al. 2018) and deformation stages, in particular concerning a possible record of Variscan deformation (Stöcklin 1968; Thiele et al. 1968; Fergusson et al. 2016; Gharibnejad et al. 2020), remain controversial. Geochronological data of metamorphic units from the Cimmerian blocks and igneous rocks from the SSZ are summarized in Fig. 2a.

The Sanandaj-Sirjan Zone (Fig. 1a, b) runs parallel to the Zagros orogen, from eastern Anatolia to the northwestern part of the accretionary wedge of Makran (McCall 2002). This zone experienced polyphase deformation and metamorphism, as shown by petrological (e.g. Khalatbari-Jafari et al. 2003; Baharifar et al. 2004, 2019; Davoudian et al. 2007, 2016; Saki et al. 2011; Moazzen et al. 2013; Sheikholeslami 2015; Sepahi et al. 2018a, b; Monfaredi et al. 2020), structural (e.g. Talebian and Jackson 2002; Mohajjel et al. 2003, 2006; Moosavi et al. 2014), and geochronological studies (Fig. 2b). In the northern Sanandaj-Sirjan Zone, metamorphic rocks related to high temperature-low pressure (HT-LP) regional metamorphism and/or inferred arc-related contact metamorphism dominate (Baharifar et al. 2004; Sarkarinejad and Azizi 2008). Several metamorphic

episodes, dated to the Precambrian (e.g. Berberian and Berberian 1981; Haghipour and Aghanabati 1989) to Cretaceous and Paleocene (e.g. Berberian and Berberian 1981; Jamshidibadr et al. 2010; Shakerardakani et al. 2015; Monfaredi et al. 2020; Fig. 2a, b) are inferred to have affected the northern SSZ. The tectono-metamorphic history of the southern SSZ is less well understood. Based on the unconformity between Late Triassic and Paleozoic and the absence of earlier Paleozoic unconformities, Sheikholeslami et al. (2003, 2008) considered the first tectono-metamorphic event to be of Eo-Cimmerian age. A Variscan event was nevertheless suspected in the SSZ based on $^{40}K$–$^{40}Ar$ radiometric ages (Fig. 2b) for the Sikhoran ($^{40}K$–$^{40}Ar$ biotite ages: ~330–301 Ma; Ghasemi et al. 2002), Dorud-Azna ($^{40}Ar$–$^{39}Ar$ amphibole ages: > 322.2 ± 3.9 Ma; Shakerardakani et al. 2016, 2017) and Kore Sefid regions ($^{40}K$–$^{40}Ar$ biotite ages: 404 ± 8, 362 ± 7 Ma; Watters et al. 1970). However, it is noteworthy that Variscan ages are never reported from high-retentivity isotopic systems (Fig. 2b). The existence of a marked contrast in maximum metamorphic temperatures between pre- and post-late Devonian rocks was also recently reported (Gharibnejad et al. 2020).

Many aspects of the structural and metamorphic evolution of the (southern) SSZ are still poorly constrained, hampering a correct assessment of its geodynamic setting and relationship with the other Cimmerian blocks, as well as with the northern SSZ. In order to elucidate these aspects, the present study focuses on retrieving the P–T evolution of metapelitic rocks from the southern Sanandaj-Sirjan Zone and relating it to meso- and large-scale structural observations. We discuss below the significance of this metamorphic evolution within the frame of the SSZ and the assembly of the Cimmerian blocks.

# Geological setting

## Tectonic overview of the Sanandaj-Sirjan Zone

The SSZ (Fig. 1a, b), forming the southwestern edge of the Central Iranian microcontinent, rifted away from northern Gondwana during the opening of the Neotethys from late Carboniferous to Permian (e.g. Takin 1972; Şengör 1984; Shakerardakani et al. 2017). The SSZ changed from a passive to an active margin when the Neotethyan north-dipping subduction started. The initiation of this subduction is inferred to coincide with the closure of the Paleotethyan ocean, either in the Late Triassic to Early Jurassic (e.g. Berberian and King 1981; Stampfli 2000; Agard et al. 2005, 2011; Mohajjel and Fergusson 2014) or in the Late Jurassic (Mohajjel et al. 2003). Fragments of continental material subducted to eclogite facies conditions at ~180 Ma and underplated at the base of the SSZ suggest active subduction during the Early Jurassic (Davoudian et al. 2007, 2016). Most studies relate the widespread ~170 Ma Mid-Jurassic
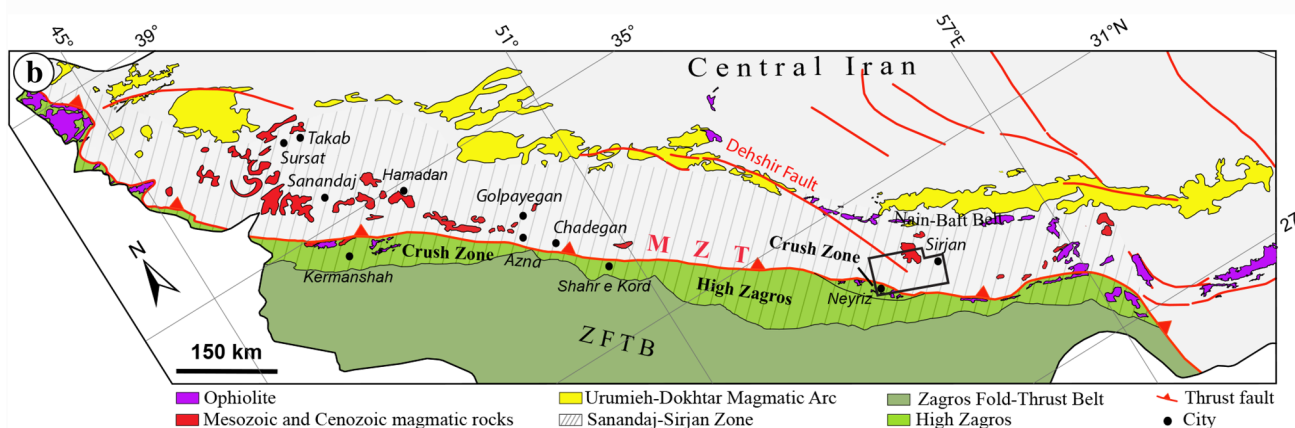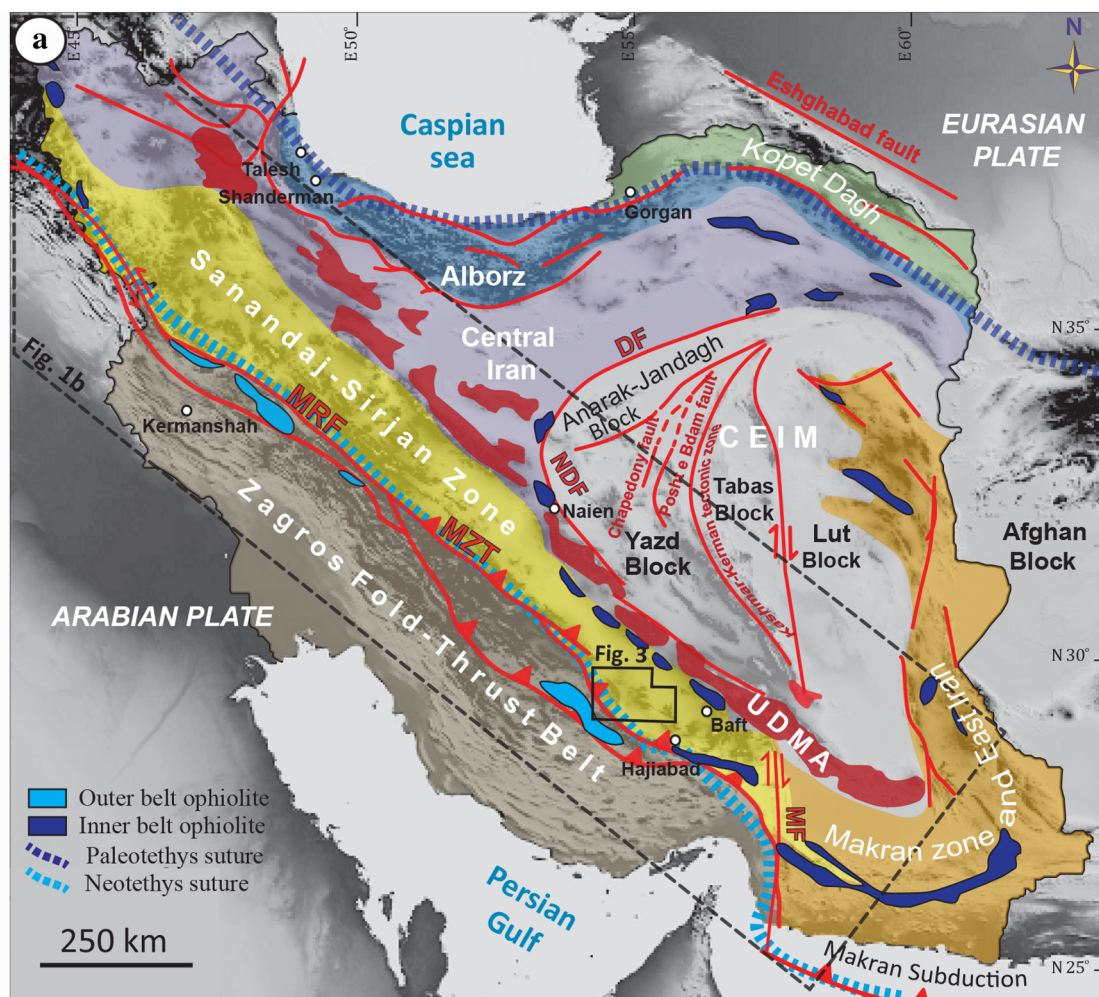
**Fig. 1** Tectonic setting of the Sanandaj-Sirjan Zone. **a** Map showing Cimmerian blocks (Central Iran, Alborz and Sanandaj-Sirjan zone), first order structures and tectonic units of the Arabian–Eurasian collisional zone in Iran (after Stöcklin and Nabavi 1969; Aghanabati and Haghipour 1975; Berberian and King 1981; Berberian 1983; Aghanabati et al. 1994a, b; Allen et al. 2003, 2011; Morley et al. 2009; Aghanabati 2013; Mohajjel et al. 2014). The location of **b** is indicated by a dashed box and the study area is shown by a black polygon. *CEIM* Central East Iranian Micro-Plate; *DF* Doruneh Fault; *MF* Minab Fault; *MRF* Main Recent Fault; *MZT* Main Zagros Thrust; *NDF* Naien-Dehshir Fault; *UDMA* Urumieh-Dokhtar Magmatic Arc. **b** Simplified tectonic map showing the major units bounding the Sanandaj-Sirjan Zone (modified after Moosavi et al. 2014). *MZT* Main Zagros Thrust; *ZFTB* Zagros Fold Thrust Belt
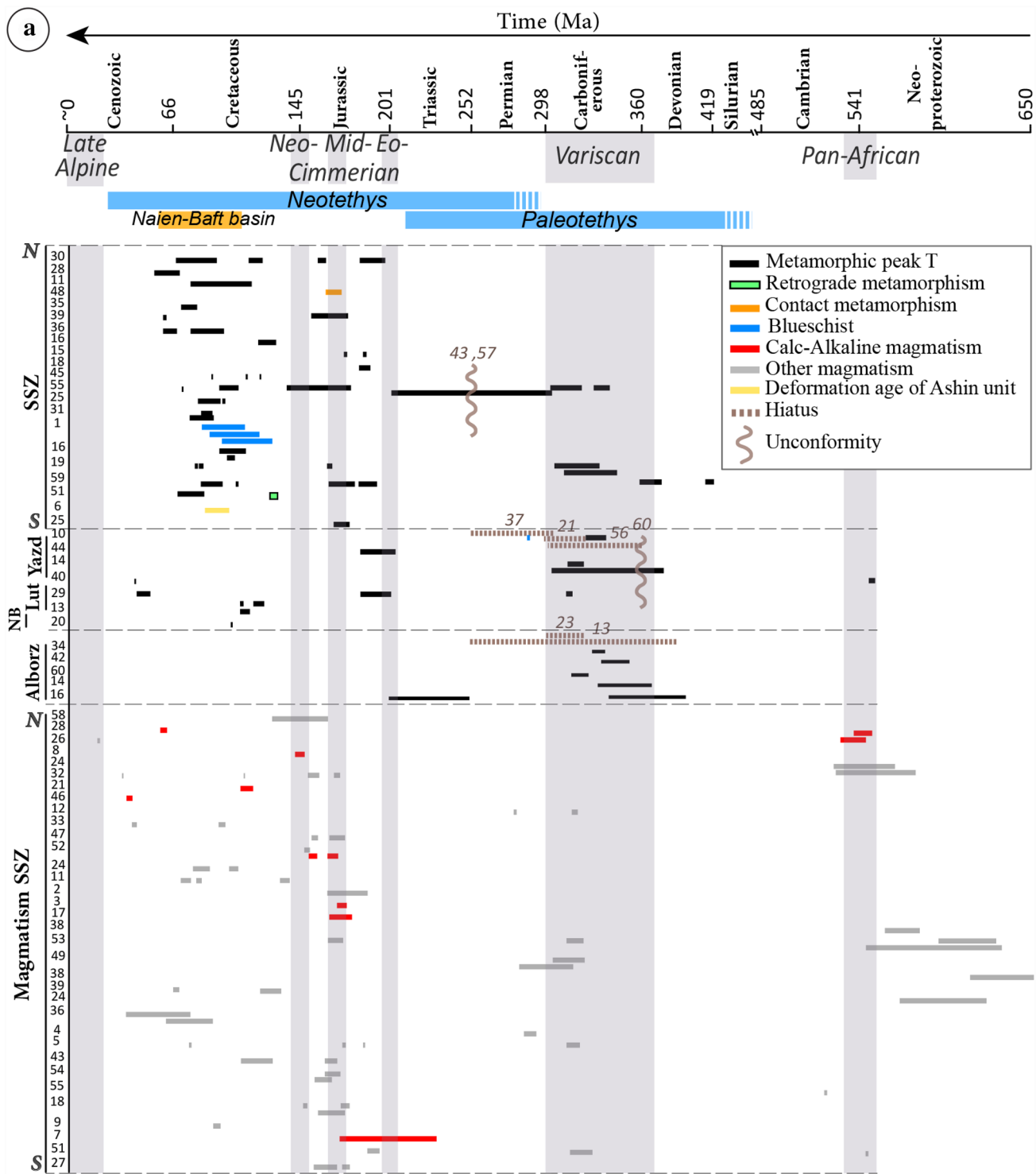
**Fig. 2** Compilation of geochronological data from structural units of Iran. **a** Summary of available radiometric ages and stratigraphic data across the Sanandaj-Sirjan zone, Central Iran (Yazd, Lut, Naein-Baft), and Alborz blocks, in addition to the age of basement and granitoids of the SSZ. The numbers on the left side of the figure are references provided in the online resource 1. **b** Geochronological data (metamorphic ages) across the SSZ, from NW to SE. Numbers along the *x*-axis correspond to the following references: (1) Agard

et al. (2006), (2) Baharifar et al. (2004), (3) Davoudian et al. (2016), (4) Delaloye and Desmons (1980), (5) Fazlnia et al. (2007), (6) Ghasemi et al. (2002), (7) Haynes and Reynolds (1980), (8) Jamshidibadr et al. (2010), (9) Monfaredi (2015), (10) Monfaredi et al. (2020), (11) Rachidnejad-Omran et al. (2002), (12) Sarkarinejad et al. (2009), (13) Sheikholeslami et al. (2003), (14) Sheikholeslami et al. (2008), (15) Watters et al. (1970) [Mineral abbreviations from Whitney and Evans 2010]
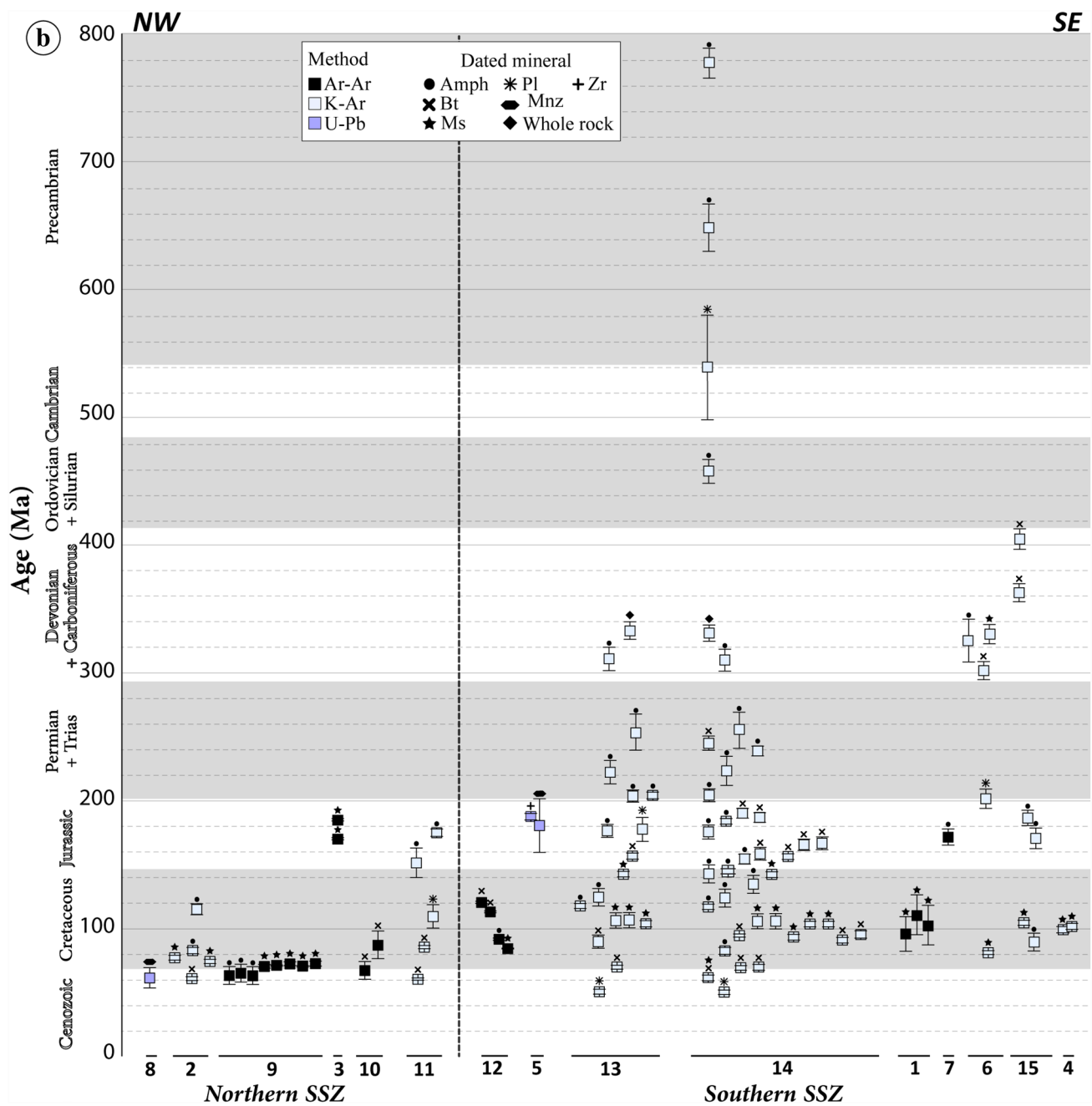
**Fig. 2** (continued)

(to locally Early Cretaceous) igneous rocks to arc magmatism above a convergent plate boundary (e.g. Berberian and Berberian 1981; Fazlnia et al. 2007, 2009, 2013; Shahbazi et al. 2010; Sepahi et al. 2018b; Fig. 2a). Based on compiled geochemical data of Sanandaj-Sirjan intrusions, including calc-alkaline granites, some studies nevertheless questioned this interpretation and considering the isotopic compositions of mafic rocks, they proposed a continental rift setting instead (e.g. Hunziker et al. 2015; Azizi and Stern 2019).

The SSZ is bounded to the southwest by the MZT (Fig. 1a, b). It represents the inner part of the Zagros orogen and structurally overlies the Crush zone (Fig. 1b), comprised of deformed sediments and obducted ophiolites (Falcon 1967; Wells 1969; Agard et al. 2005). The SSZ exposes Permian and Mesozoic rocks together with rarer pre-Permian basement (e.g. Crawford 1977; Sheikholeslami et al. 2003; Hassanzadeh et al. 2008; Hosseini et al. 2012; Shafaii Moghadam et al. 2016; Fig. 2a). Radiochronological data (Fig. 2a) also attest to the existence of Precambrian basement outcrops (Haghipour and Aghanabati

1989; Stockli et al. 2004; Hassanzadeh et al. 2008; Horton et al. 2008; Jamshidibadr et al. 2013; Shakerardakani et al. 2015, 2019; Moradi et al. 2020). U–Pb dating of zircons revealed a whole range of crystallization ages for intrusive rocks, from Archean (U–Pb: ~2.7 Ga; Shakerardakani et al. 2015) to Paleoproterozoic (U–Pb: ~1.8–1.7 Ga; Shafaii Moghadam et al. 2016) and late Neoproterozoic (e.g. Hassanzadeh et al. 2008; Nutman et al. 2014).

In spite of its lateral continuity, all along the Zagros orogen, some first-order differences described below, characterize the northern and southern SSZ, i.e. north and south of the Dehshir fault (Fig. 1a) as follows:

(i) Erosion and exhumation were greater in the southern SSZ, where Paleozoic units dominate, whereas units exposed in the northern SSZ are mostly Jurassic and Permo-Triassic.

(ii) The thick Permo-Triassic (and possibly up to Jurassic; Hassanzadeh and Wernicke 2016) basin of the Hamadan phyllites is mostly found in the northern SSZ.

(iii) Arc magmatism, in the north, is not only Jurassic as throughout the entire SSZ but also extends into the Cretaceous (e.g. Moritz et al. 2006; Heidari et al. 2015; Fig. 2a).

(iv) Eclogite facies continental rocks of Mid-Jurassic age ($^{40}Ar$–$^{39}Ar$ ages: ~184–172 Ma; 590–630 °C, 21–24 kbar; Davoudian et al. 2007, 2016) are only found in the northern SSZ.

(v) A Late Cretaceous back-arc domain is inferred to be preserved (i.e. the Naien-Baft ophiolite; Fig. 1a, b; e.g. Shafaii Moghadam and Stern 2015; Shirdashtzadeh et al. 2020) only in the southern SSZ, whereas the Paleocene fore-arc is only located in the northern SSZ (Kermanshah ophiolite; Fig. 1a, b; Whitechurch et al. 2013).

(vi) Radiometric ages in the southern SSZ show a much larger scatter compared to its northern counterpart (Fig. 2b).

## Tectono-metamorphic evolution of the southern SSZ

Assuming that the existing radiometric data of the SSZ correctly track past tectono-metamorphic events, their large scatter in the southern SSZ points to a complex, polyphase metamorphic evolution from the Devonian to the Late Cretaceous (~400 to ~60 Ma; Watters et al. 1970; Sheikholeslami et al. 2003, 2008; Sarkarinejad et al. 2009; Fig. 2b). Radiometric ages in the southern SSZ cover the entire range from Precambrian to early Cenozoic, whereas they are limited between Jurassic and early Cenozoic in the northern SSZ (Fig. 2b). However, dated samples in the northern SSZ consist of a significantly smaller number compared to the

southern SSZ. Thus the difference may only result from a sampling bias. Some metamorphic ages reported by Sheikholeslami et al. (2008) including abnormal $^{40}K$–$^{40}Ar$ data (e.g. ~777 and 650 Ma) point to the occurrence of metamorphism during the Neoproterozoic, whilst U–Pb age data (Sheikholeslami, 2002; Safarzadeh et al., 2016) indicate the existence of a Precambrian basement (~580–520 Ma) in the SSZ. Within our study area, near Sirjan (Fig. 1b), previous authors identified amphibolite-facies, km-scale recumbent folds affecting Paleozoic rocks, later overprinted by tight to isoclinal folds (Sarkarinejad 2007; Sarkarinejad et al. 2009; Sarkarinejad and Keshavarz 2010; Sheikholeslami et al. 2008). Sheikholeslami et al. (2008) recognized three distinct foliations (S1–S3) associated with three successive fold generations showing mainly NW–SE to E–W trending axes. The few available P–T estimations from this area (Sheikholeslami 2002: ~10 kbar, ~700 °C; Fazlnia et al. 2007; 9.5 ± 1.2 kbar, 705 ± 40 °C; Rahimi et al. 2021: 3–6 kbar, 548–710 °C) have not yet been linked to the above structures and fabrics. Based on the existence of an angular unconformity between Paleozoic metamorphic rocks and Jurassic (meta)sedimentary units, and on structural investigations advocating for the existence of two main deformation stages, Sheikholeslami (2015) proposed that two syntectonic metamorphic phases affected the southern SSZ. The first, which attained amphibolite facies conditions, was followed by a greenschist-facies phase. These phases were suggested to have occurred during the Late Triassic Eo-Cimmerian and post Eo-Cimmerian events, respectively (Sheikholeslami 2015). The age of the latter stage was inferred from the deformation contrast between the schistose Jurassic rocks and the only mildly deformed and unconformable Cretaceous Orbitolina limestones above (~135 Ma; Ricou 1974). In the Kore Sefid area (Fig. 3), Sheikholeslami et al. (2008) and Fazlnia et al. (2009) reported a Barrovian metamorphic paragenesis, marked by the presence of garnet ± kyanite ± staurolite in metapelites and garnet-bearing amphibolites, which they linked to the first (and most severe) Eo-Cimmerian deformation event. This regional-scale Barrovian metamorphism predated the Early Jurassic since these units are cross-cut by the ~185 Ma S-type granites of the Chah Dozdan batholith (Fig. 3). Fazlnia et al. (2007) reported the emplacement of magma into the metamorphic rocks resulted in the existence of metapelitic xenoliths within the intruded magma. The exact age of the amphibolite-facies metamorphism is still unclear. Southeast of our study area, the Sikhoran complex, east of Hajiabad (Fig. 1a), mostly consisting of mafic and ultramafic rocks (Ricou 1974), experienced lower amphibolite facies metamorphism probably during the Carboniferous (i.e. $^{40}K$–$^{40}Ar$ biotite ages of ~301, 324 and 329 Ma; Ghasemi et al. 2002; Fig. 2b). In contrast, for the amphibolites of the Bahrame Gour area (eastern Qatruyeh; Fig. 3), Rahimi et al. (2021) obtained a pre-Middle Jurassic metamorphic
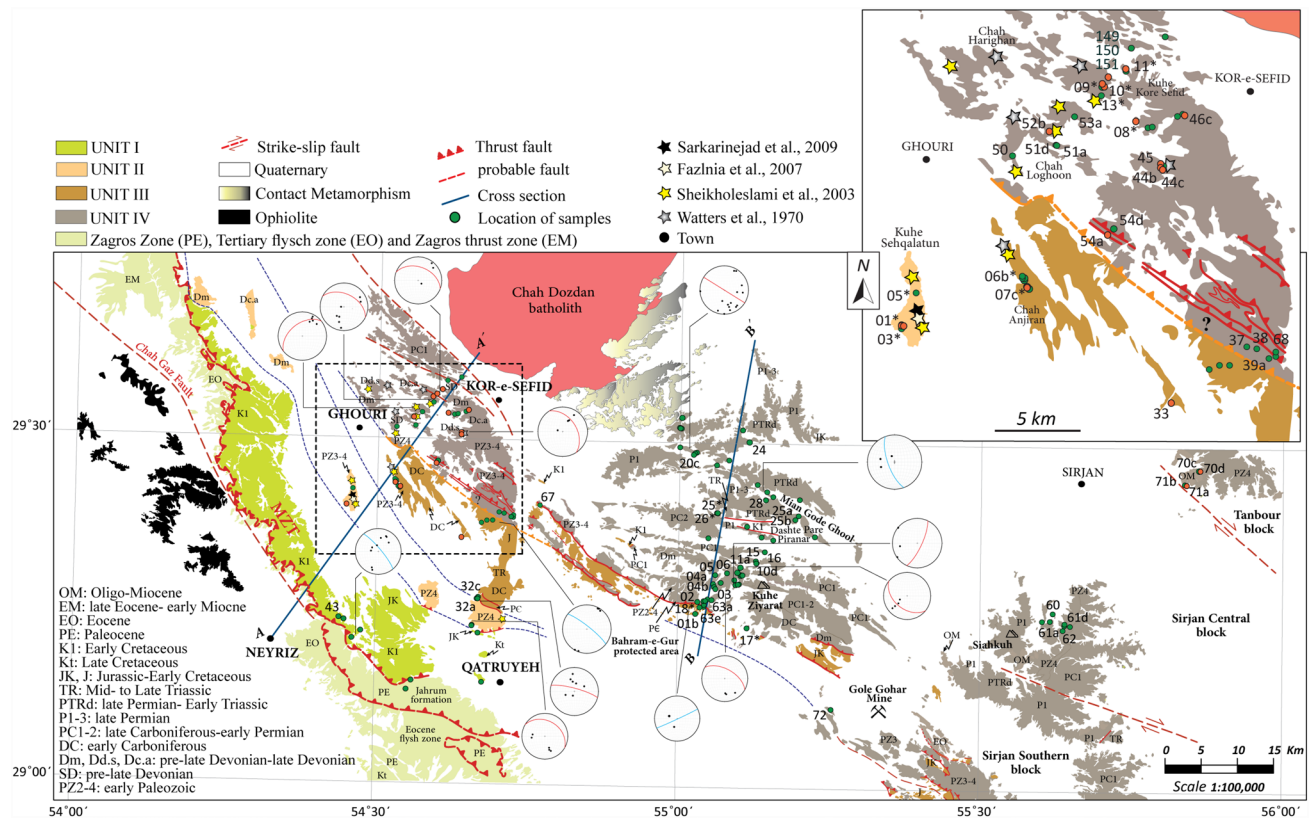
**Fig. 3** Simplified geological map of the southern SSZ (based on the Sirjan, Zardu, Gole Gohar, Kore Sefid, Qatruyeh, Neyriz and Chahak 1:100,000 maps published by Geological Survey of Iran; Sabzehei et al. 1994a, b, 1995, 1996, 1997a, b, 1999), showing the trace of cross-sections (AA′ and BB′) of Fig. 4, and the position of samples (green circles). Analyzed samples are shown in red and the sites of radiometric ages from previous studies are shown by open stars. White areas on the map represent the Quaternary cover. The blue dotted lines mark the contacts between the tectonic units described in the text. On the stereonets (lower hemisphere equal-area projection), the red and blue circles illustrate F2 and F3 axial planes respectively, and the black dots show the poles to foliations. The orange dashed line highlights the tectonic boundary between UNIT III and UNIT IV

age ($^{40}Ar$–$^{39}Ar$ amphibole age: > 162 Ma) and argued for a continental within-plate setting for the metamorphic event.

Later metamorphic episodes were suspected to the west of our study area (Sehqalatun massif; Fig. 3), where Cretaceous $^{40}Ar$–$^{39}Ar$ ages (~ 119–112 Ma and ~ 91 Ma; Fig. 2b) were interpreted by Sarkarinejad et al. (2009) to reflect subduction-related metamorphism. Exhumation of blueschists and changes in the subduction regime are indeed reported across the ~ 100–80 Ma period in the southern SSZ (Agard et al. 2006; Monié and Agard 2009; Angiboust et al. 2016; Fig. 2a). Later thrusting associated with collisional movements started from the Oligocene onwards (Omrani 2008; François et al. 2014).

While no unconformity has so far been reported between the early and late Paleozoic formations, a metamorphic temperature gap between early Paleozoic (up to Devonian) units ($T > 500$ °C) and late Devonian to Cretaceous ones ($T < 400$ °C) was detected using the Raman spectroscopy of carbonaceous material (Gharibnejad et al. 2020).

# Tectono-metamorphic evolution of the northern SSZ

The northern SSZ provides extensive exposure of deformed metamorphic rocks, particularly near Hamadan, Golpayegan, and in the Mahnehshan complex, near Takab (Fig. 1b), where peak-burial attained ~ 600 °C and 7 kbar (Saki et al. 2011). In the Hamadan area, HT-LP regional metamorphism is marked by garnet ± staurolite-bearing micaschists, commonly containing andalusite and/or sillimanite (and kyanite in places; Baharifar et al. 2004; Sepahi et al. 2004, 2013; Agard et al. 2005). Estimated P–T conditions of these rocks lie in the 4–5 kbar and 550–700 °C range (Sepahi et al. 2018a; see Monfaredi et al. 2020 for a review). Part of the regional metamorphic parageneses, documented in the northern SSZ has been overprinted by contact metamorphism related to the extensive ~ 170 Ma Mid-Jurassic intrusions (e.g. Alvand batholith; Shahbazi et al. 2010; Sepahi et al. 2018b: $^{40}Ar$–$^{39}Ar$: ~ 168–149 Ma; Monfaredi et al. 2020).

Despite some age constraints, the timing of regional HT-LP metamorphism is still unclear. While it does not affect Jurassic rocks, it overprinted the Hamadan phyllites whose age is still disputed (see Monfaredi et al. 2020 for a review). The protoliths of these phyllites formed as part of a large Permo-Triassic basin following Neotethys rifting, and they are younger than ~ 270 Ma (Fergusson et al. 2016), but may extend up to the Jurassic, i.e. across the Late Triassic Eo-Cimmerian event (Hassanzadeh and Wernicke 2016). From the structural view, Mohajjel et al. (2006) attributed metamorphism of the Hamadan phyllites (and related S1 fabrics) to the Neotethyan subduction during Late Jurassic-Early Cretaceous, and Fergusson et al. (2016) identified two NW–SE striking fold generations north of Azna (Fig. 1b), which they related to Late Triassic Eo-Cimmerian movements. Based on textural evidence, Monfaredi et al. (2020) outlined the existence of three metamorphic events called M1–M3. The exact age and P–T conditions of the older M1 metamorphic stage, which is characterized by garnet-bearing metamorphic mineral assemblages, are unknown. M2 is a contact metamorphic event related to the Alvand intrusions, which overprinted the M1 assemblages and is dated 170–160 Ma (e.g. Zircon U–Pb ages: Shahbazi et al. 2010: $171.1 \pm 1.2$ and $153.3 \pm 2.7$ Ma; Chiu et al. 2013: $165.1 \pm 2$ and $163.9 \pm 1.8$ Ma; Monazite U–Pb ages: Sepahi et al. 2018b: 172–162 Ma, 2019: zircon U–Pb ages: $173.6 \pm 3.1$ Ma). M3 is characterized by andalusite-staurolite-sillimanite, and it provided surprisingly young $^{40}Ar–^{39}Ar$ white mica ages, in the range ~ 75–65 Ma (Monfaredi et al. 2020), yet consistent with ages reported from the Hamadan area by Baharifar et al. (2004; ~ 63 Ma monazite overgrowths, also recorded in hornfels). This metamorphism was attributed to the Late Cretaceous exhumation of the Hamadan metamorphic rocks due to extension along a major ductile normal fault (Monfaredi et al. 2020). In the Golpayegan region (northern SSZ; Fig. 1b), structural studies and geochronological data (Moosavi et al. 2014: $^{40}Ar–^{39}Ar$ biotite and amphibole ages: ~ 110–60 Ma) of similar Late Cretaceous–early Paleocene age are inferred to date the formation of recumbent isoclinal (Moritz et al. 2006) and open upright folds.

In summary, some ambiguity remains on the tectono-metamorphic evolution, depending on whether the HT-LP ~ 75–65 Ma M3 ages mark the timing of peak metamorphism or of the possibly extension-related retrogression (Monfaredi et al. 2020). Even a younger age of Barrovian metamorphism was proposed based on geochronological data from the Sursat complex (Fig. 1b), where zircon and monazite U–Pb ages yielded ~ 605 and ~ 61 Ma. These data were inferred to, respectively, represent the Precambrian depositional age of sedimentary protoliths and the occurrence of peak Barrovian metamorphism in the Paleocene (Jamshidibadr et al. 2010). If the M3 metamorphic event is confirmed to be distinct from the M1 and M2 events, its formation before the onset of the Arabia–Eurasia collision still needs to be explained.

## Tectono-metamorphic evolution in adjacent Cimmerian blocks

### - Alborz

Amongst the Cimmerian blocks, the Alborz range (Fig. 1a) best preserves the record of Paleotethys closure during the Eo-Cimmerian (e.g. Stöcklin 1974b; Horton et al. 2008), as exemplified by the calc-alkaline magmatic rocks, ophiolitic complexes and the Carboniferous Shanderman (Fig. 1a) subduction-related eclogitic complex (e.g. Takin 1972; Stöcklin 1974b; McCall 1997; Dilek and Newcomb 2003; Stern 2005; Zanchetta et al. 2009; Zanchi et al. 2009; Omrani et al. 2013; Rossetti et al. 2017; Fig. 2a). The location of the Paleotethys suture (Fig. 1a; Alavi 1996; Jackson et al. 2002; Allen et al. 2003) is highlighted by metamorphic rocks and ophiolites discontinuously exposed from the east (Gorgan region; Fig. 1a) to the west (Talesh Mountains; Fig. 1a; e.g. Allen et al. 2003; Stern 2005; Zanchetta et al. 2009; Dilek and Furnes 2011). Following the closure of the Paleotethys, deposition of the post-collisional Late Triassic-Middle Jurassic Shemshak formation marks the major unconformity in the area (Seyed Emami 2003; Fursich et al. 2005), as throughout most of Central Iran (Stöcklin 1968).

### - Central Iran and Lut blocks

The Central Iranian microcontinent, which comprises the fault-bounded Lut, Tabas and Yazd tectonic blocks (Fig. 1a; e.g. Takin 1972; Berberian and King 1981; Soffel et al. 1996; Bagheri and Stampfli 2008; Allen et al. 2011), exposes several metamorphic complexes recording Pan-African, possibly Variscan, Cimmerian and Alpine episodes (e.g. Chapedony, Boneh Shourow, Tashk, Saghand and Sarkuh massifs; Huckriede et al. 1962; Ramezani and Tucker 2003; Bagheri and Stampfli 2008; Kargaranbafghi et al. 2015).

In the northern Yazd block (Fig. 1a), late Carboniferous (~ 330–320 Ma; Bagheri and Stampfli 2008; Fig. 2a), blueschist facies subduction-related metamorphism with conditions reaching 350–400 °C and 9 kbar was documented in the Anarak and Jandaq complexes (Bagheri and Stampfli 2008; Zanchi et al. 2009, 2014; Buchs et al. 2013). Elsewhere in Central Iran, based on U–Pb data, inferred peak metamorphic ages of amphibolite facies basement rocks (e.g. Boneh Shurow and Chapedony metamorphic complexes), range from the late Neoproterozoic to the Eocene (Ramezani and Tucker 2003: ~ 547 to ~ 44 Ma; Fig. 2a). Most radiometric ages cluster around 540 and 210 Ma (Ramezani and Tucker 2003),

but important spatial contrasts are visible. Dominantly Variscan (~ 380–300 Ma) $^{40}Ar$–$^{39}Ar$ white mica ages were obtained west of the Chapedony fault (Fig. 1a; Kargaranbafghi et al. 2015). In contrast, to the east of this fault, the Poshte Badam and Boneh Shurow metamorphic complexes yielded Cimmerian metamorphic ages ($^{40}Ar$–$^{39}Ar$ white mica ages: ~ 170 and 205 Ma; Kargaranbafghi et al. 2015). In the same area, along the Kashmar-Kerman tectonic zone (Fig. 1a) separating the Tabas and Yazd blocks, Masoodi et al. (2013) reported three age clusters: at ~ 200 Ma, at 170–165 Ma and at 140–130 Ma, which they attributed, respectively, to continental accretion of the Tabas and Yazd blocks during the Late Triassic–Early Jurassic Eo-Cimmerian collision, to a mid-Cimmerian event and to a late Cimmerian–Early Cretaceous compression. In northern Central Iran, Rahnati Ilkhchi et al. (2010), Rahmati Ilkhchi et al. (2011) reported the existence of Barrovian metamorphism (7–8 kbar, ~ 650 °C) of mid-Cimmerian age ($^{40}Ar$–$^{39}Ar$ age dating of muscovite: ~ 166 Ma) affecting the Late Triassic–Early Jurassic Shemshak Formation, and sealed by the Mid-Jurassic conglomerates. Further to the east, in the Lut block (Anjul area), U–Pb zircon ages, and Rb–Sr biotite and feldspar age data indicate the occurrence of possibly Mid-Jurassic and Cretaceous Barrovian metamorphic events (170 and 110 Ma; Bröcker et al. 2014; Fig. 2a).

# Structural observations in the southern Sanandaj-Sirjan zone

## Large scale structures

Based on metamorphic grade, deformation patterns, and stratigraphic age, we subdivided the study area into several tectono-metamorphic and tectono-sedimentary domains. For this purpose, we follow the interpretation of Gharibnejad et al. (2020), who inferred that the Jurassic units of the 1:100,000 Qatruyeh map (Geological Survey of Iran; Sabzehei et al. 1999) should be attributed to the Paleozoic, based on their deformation style (tight to isoclinal folds), metamorphic temperature (Raman $T > 500$ °C), and the absence of any stratigraphic or paleontological evidence in support of Jurassic age. Assuming that this interpretation is correct, a relatively continuous age succession of metasedimentary units is observed, younging from southwest to northeast.

Our study area in the southern SSZ can be defined as the stack of four major tectonic units, which we describe below from bottom to top, hence from south to north (Figs. 3, 4) as follows:

(i) The first unit (UNIT I; Fig. 3) consists of Late Jurassic–Early Cretaceous (JK) and Cretaceous (K1) beds, in addition to Tertiary units (Paleocene–Eocene and
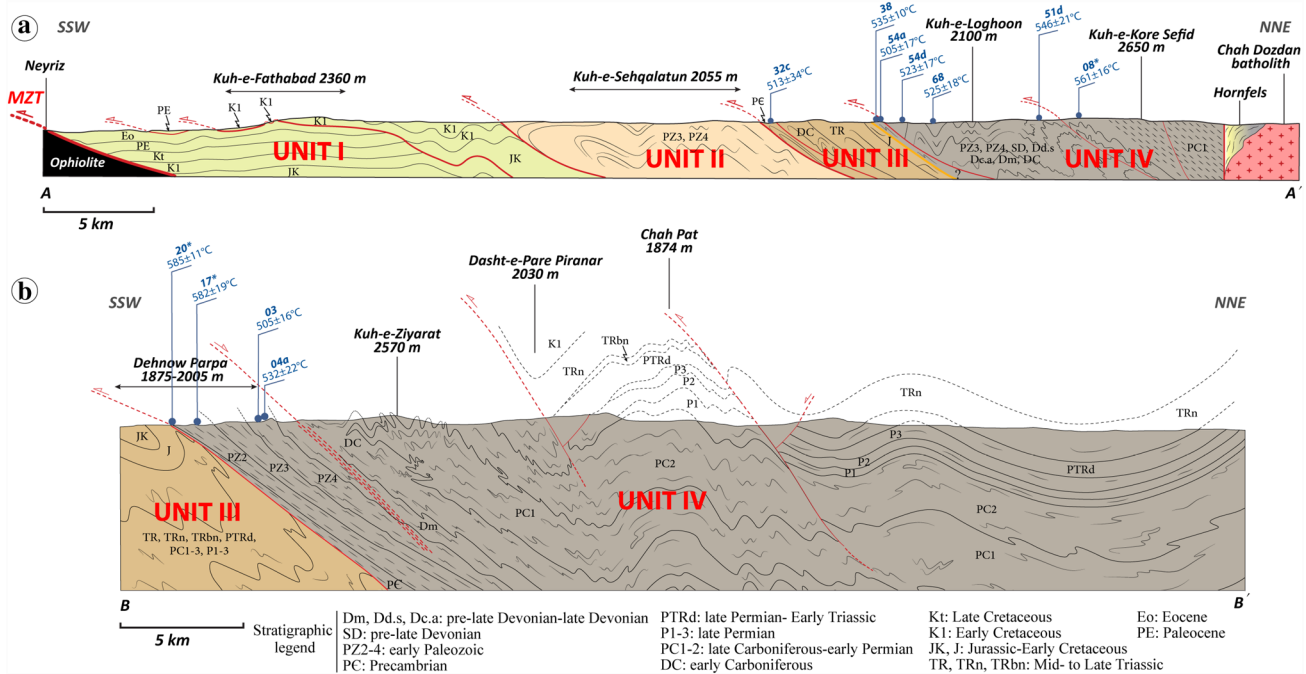


**Fig. 4** Cross-sections of the southern SSZ. Traces of sections are shown in Fig. 3. The interpretation of **b** at depth is only based on the extrapolation of surface data, without any independent geophysical information. The numbers indicate maximum temperatures based on Raman data from Gharibnejad et al. (2020). Sample numbers are bold, and more details are provided in Table 1. The boundary between UNITs III and IV is shown by the orange fault

Eocene–Oligocene; PE and EO in Fig. 3). Within this unit, two major thrusts are present: one bringing the Paleocene (PE) on top of the Eocene (EO) and one further north, bringing the Cretaceous (K1) on top of the Eocene (Fig. 4a). As shown in the cross-section of Fig. 4a the latter thrust cross-cuts the former one, and because it is in a more internal position we interpret it to be an out-of-sequence thrust. Based on map evidence (1:100,000 geological map of Neyriz by Geological Survey of Iran; Sabzehei et al. 1996) a total displacement of at least 7 km of the Cretaceous Orbitolina limestone (K1) over the Tertiary (Eocene–Oligocene) flysch must have taken place (Fig. 3). The early Paleocene–Eocene Jahrum formation (PE unit; Fig. 3) was also thrust above the Tertiary flysch Zone (mainly EO units) over a similar distance. To the northeast of the Gole Gohar area (Dashte Pare Pire Anar region; Fig. 3), the Cretaceous limestone (K1) lies below the Late Triassic metasedimentary and volcanic units (TR). Because the major thrust accommodating displacement of the Cretaceous (K1, Fig. 4a) above the Eocene appears to be a thin-skinned structure, we included both sedimentary sequences within one single tectonic unit (UNIT I).

(ii) Immediately above UNIT I, lies UNIT II, consisting of early Paleozoic sequences (PZ3, PZ4) thrust over Early Cretaceous units (K1) in the eastern Neyriz area (Figs. 3, 4a). Although poorly exposed at the surface, a few outcrops of early Paleozoic units are observed in the northwestern lateral continuation of the aforementioned ones. These Paleozoic units are also located north of Unit I; thus we included them in Unit II. Hence the lateral extent of Unit II may be very large in our study area. The main contacts within these areas are sub-parallel to the general strike of the SSZ (e.g. in the Qatruyeh and Neyriz maps).

(iii) Northeastern of Qatruyeh (Fig. 3) mafic to ultramafic Precambrian rocks (PЄ; Fig. 4a) are locally exposed and lie above the early Paleozoic rocks (PZ4; Fig. 4a) of Unit II. They form the base of a third tectonic unit (Unit III), which grades into a late Paleozoic series (mainly early Carboniferous–late Devonian; DC) overlain by Triassic-Jurassic rocks (TR), as shown by a continuously exposed section north of Qatruyeh. The section north of Qatruyeh is the only one allowing for continuous exposure of Unit III in our study area (Fig. 3).

(iv) The structurally highest unit (UNIT IV) covers the largest part of our study area (Figs. 3, 4) and presents a roughly continuous sequence from the Precambrian (PЄ; Fig. 4b) to the Cretaceous (K1; Fig. 4b).

It includes a thin, hundred meter thick Precambrian sequence at its base (PЄ; Fig. 4b), only observed in the area of Dehnow Parpa, where it is thrust above the Jurassic sequence (J; Fig. 4b) of Unit III. Almost complete Paleozoic (PZ2, PZ3, PZ4, P1, P2, P3) and Mesozoic sequences, up to the Cretaceous (K1), overlie the latter Precambrian (PЄ). Where the Precambrian unit is missing, the base of Unit IV consists of early Paleozoic rocks (PZ2; Fig. 4b).

The presence of the structurally highest units in the northern and eastern parts of the investigated area and the absence of discrete structures oblique to the SSZ to mark their boundaries possibly indicate a lateral, differential exhumation related to the northeastern dip of all structures.

## Folding phases

Two major phases of folding, and possibly an older and poorly preserved one, can be recognized in the study area, both at the outcrop- and km-scale. The first of the two major phases are characterized by km-scale, tight folds (Fig. 5a–c) showing significant internal ductile deformation of the layers, (Fig. 6a), leading to thickening of fold hinges compared to fold limbs. Based on field and map observations, these folds seem to affect all stratigraphic units up to the Permo-Triassic (late Permian-Early Triassic; PTRd in UNIT IV; Fig. 5a), but they are not observed in the Jurassic and post-Jurassic series (provided the Jurassic units are defined as in Gharibnejad et al. 2020; Fig. 6b), suggesting that they are pre-Jurassic. Because the axial planes of these structures often strike parallel to the elongate topographic ranges of the study area, these folds appear to be recumbent; however, their axial planes dip at an angle of at least 30°, in a direction that varies from SSW to NNE (Figs. 5a–c, 6c), and hence the folds are reclined. Similarly, the trend of the fold axes varies significantly, between WNW–ESE and NW–SE (Fig. 7c, d). Mesoscopic parasitic folds in thin layers usually affect the limbs of these folds (Fig. a in the online resource 2). Within some of these folds, we find local evidence of a refolded schistosity (Figs. b, c and f of online resource 2), suggesting the presence of a folding phase prior to this major folding event. Since this older phase displays a similar geometry as the pervasive, large-scale tight-to isoclinal folds (Figs. b from online resource 2 and 6d), and it is rarely exposed, recognizing this first phase is challenging. Nevertheless, based on its local presence, we define it as a F1 phase, which produced a S1 schistosity that is only visible as relics in some microlithons (Figs. c, f of online resource 2) or as inclusion trails in porphyroclasts (Fig. 8g). As a consequence, the large-scale tight folds described above belong to the second phase (F2). Where the phyllosilicate content of F2-folded lithologies is abundant, an axial plane schistosity
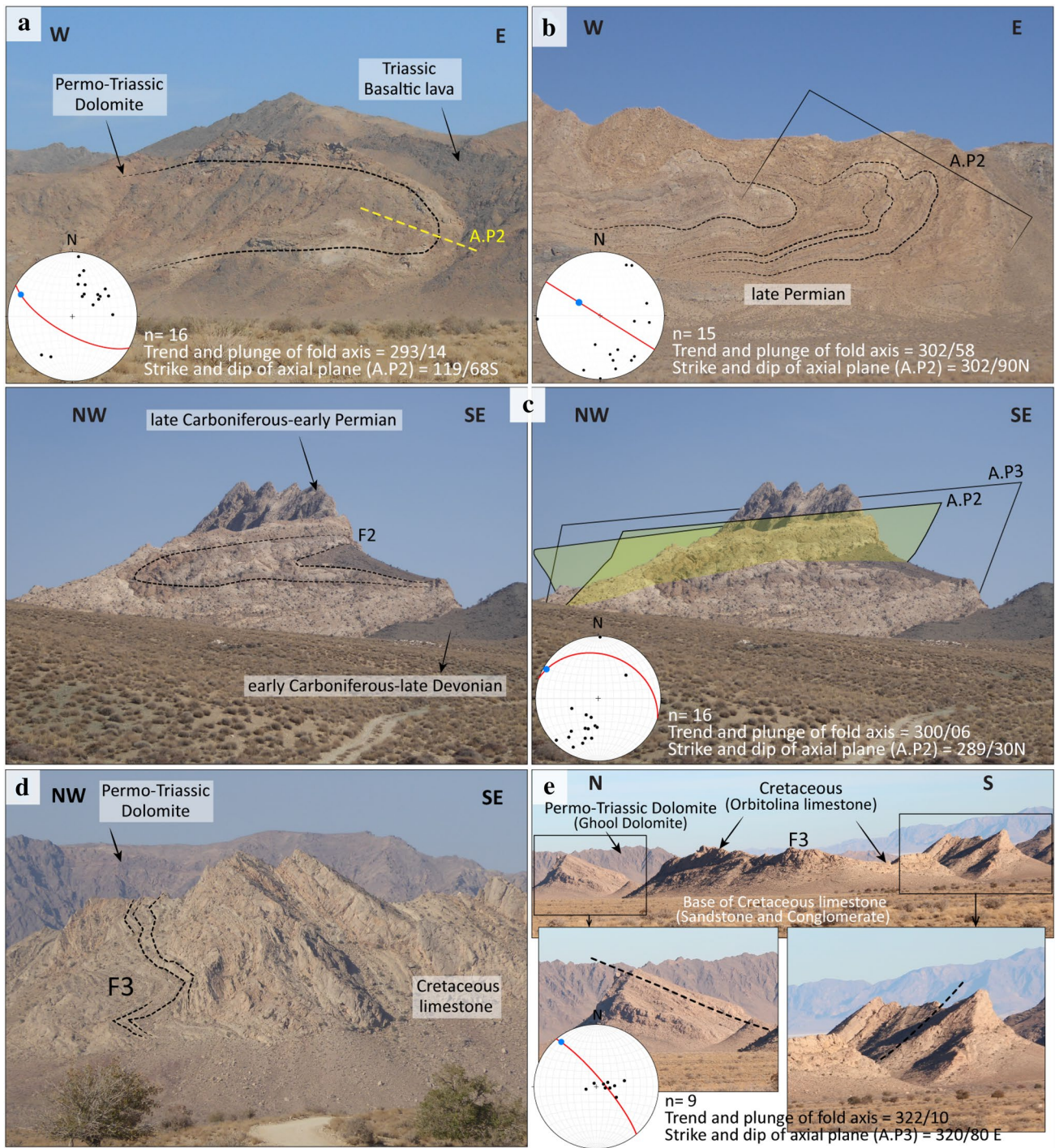
**Fig. 5** Representative large-scale folds of the southern SSZ with stereographic projections of bedding planes. **a** Isoclinal folds (F2) within late Permian-Early Triassic dolomitic units of UNIT IV, at Mian Gode Ghool (northern Gole Gohar region; Fig. 3; 29° 25′ 10″ N, 55° 11′ 58″ E). **b** F2 fold affecting late Permian units of UNIT IV (northwestern Gole Gohar area; 29° 29′ 07″ N, 55° 01′ 24″ E), **c** Isoclinal folds (F2) of Permo-Carboniferous (PC of UNIT IV) in the eastern part of the investigated area (Gole Gohar region; 29° 18′ 45″ N, 55° 06′ 04″ E). The yellow planes sketched illustrate the D2 axial plane, which is folded around the transparent, steep F3 axial plane, also striking NW–SE. **d** F3 syncline of Cretaceous, Orbitolina limestone of UNIT IV in Dashte Pare Piranar (29° 21′ 43″ N, 55° 08′ 52″ E). **e** Open, parallel F3 syncline, folding Cretaceous Orbitolina limestone (K1 of UNIT IV) in the eastern part of the study area (Gole Gohar region; 29° 22′ 53″ N, 55° 06′ 42″ E). Lower hemisphere stereonets illustrate poles to foliations (black dots), axial plane orientation (red great circle) and fold axis (blue dot)
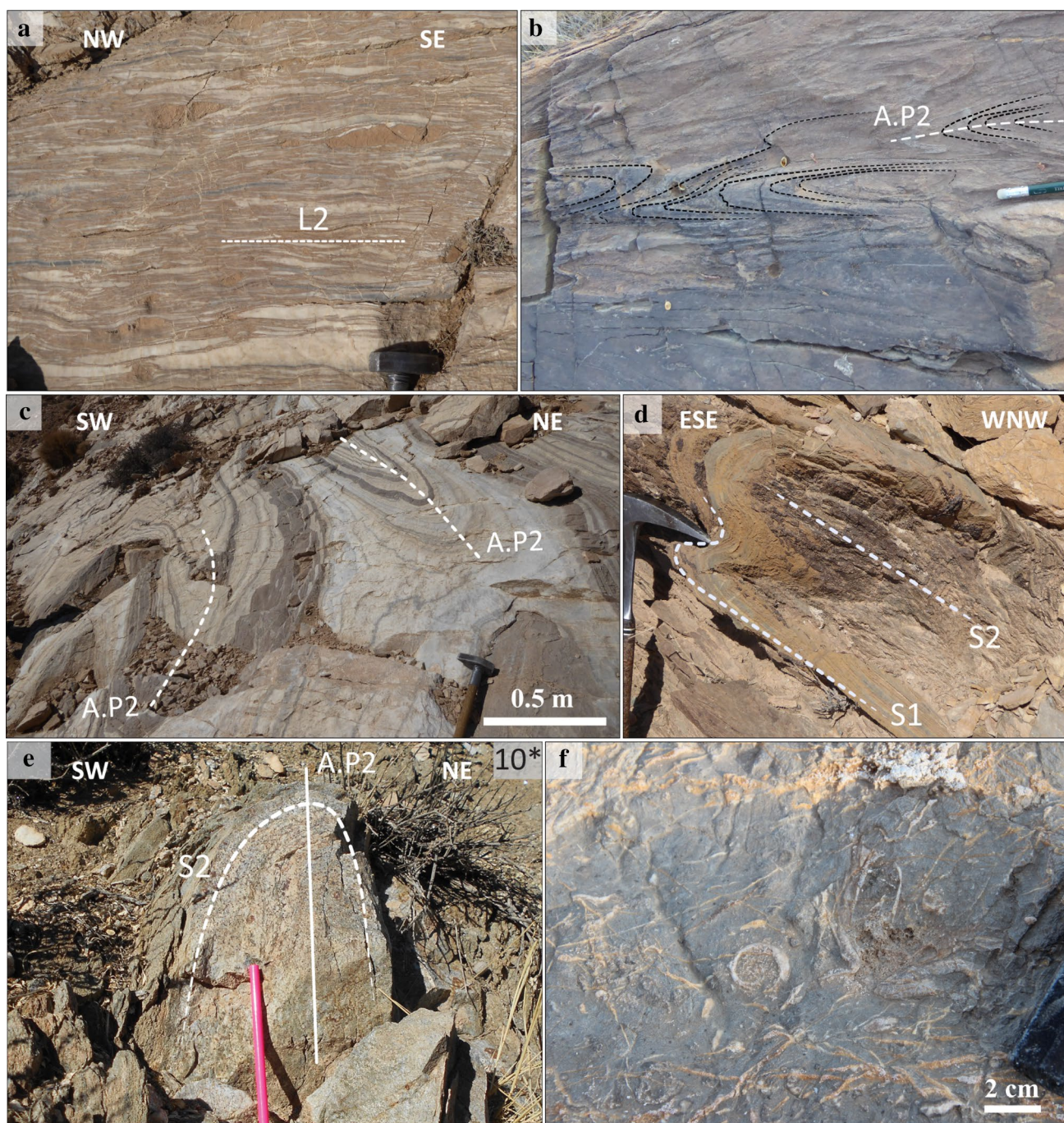
**Fig. 6** Representative outcrops of deformation structures across the study area. **a** Dolomitic marble showing intense stretching as a result of ductile flow within the lower limb of isoclinal fold shown in Fig. 5c (29° 18′ 34″ N, 55° 06′ 11″ E). **b** Isoclinal folds (F2) in the metasedimentary Jurassic units in the Qatruyeh area (UNIT IV; 29° 23′ 35″ N, 54° 42′ 37″ E), **c** Slightly refolded F2 folds in early Paleozoic marble units (pre-late Devonian; south of Kuh-e-Kore Sefid; UNIT IV; 29° 32′ 30″ N, 54° 38′ 58″ E). The F2 folds are tight to isoclinal with E–W to NW–SE striking axial planes. **d** Foliations in early Paleozoic units (PZ4 layers of UNIT II) of the south-

ern Qatruyeh area (alternation of marble and schist; 29° 13′ 49″ N, 54° 39′ 34″ E). Isoclinal F2 fold, folding S1, showing an S2 axial plane foliation. **e** Folding (F2) of garnet micaschist within pre-late Devonian-late Devonian rocks of UNIT IV (Kore Sefid area; 29° 33′ 36″ N, 54° 35′ 23″ E). **f** Undeformed fossils within unmetamorphosed Cretaceous limestone of UNIT IV, in the Gole Gohar region. The outcrop is located inside the limb of the syncline at Dashte Pare Piranar (29° 22′ 46″ N, 55° 06′ 46″ E), shown in Fig. 5e. Calcite veins suggest brittle deformation conditions

**Fig. 7** Orientation of structural data on lower hemisphere equal-area stereonets. **a** Poles to S2 schistosity. Note that all foliation poles define a NNE–SSW trending belt on the stereonet which points to a sub-horizontal WNW–ESE trending fold axis. **b** Poles to S3 axial plane schistosities, **c** fold axes (F2), **d** fold axes (F3), **e** L2 (early Paleozoic) and L3 (late Paleozoic and Jurassic) mineral lineations. The structural data are color-coded according to their stratigraphic units
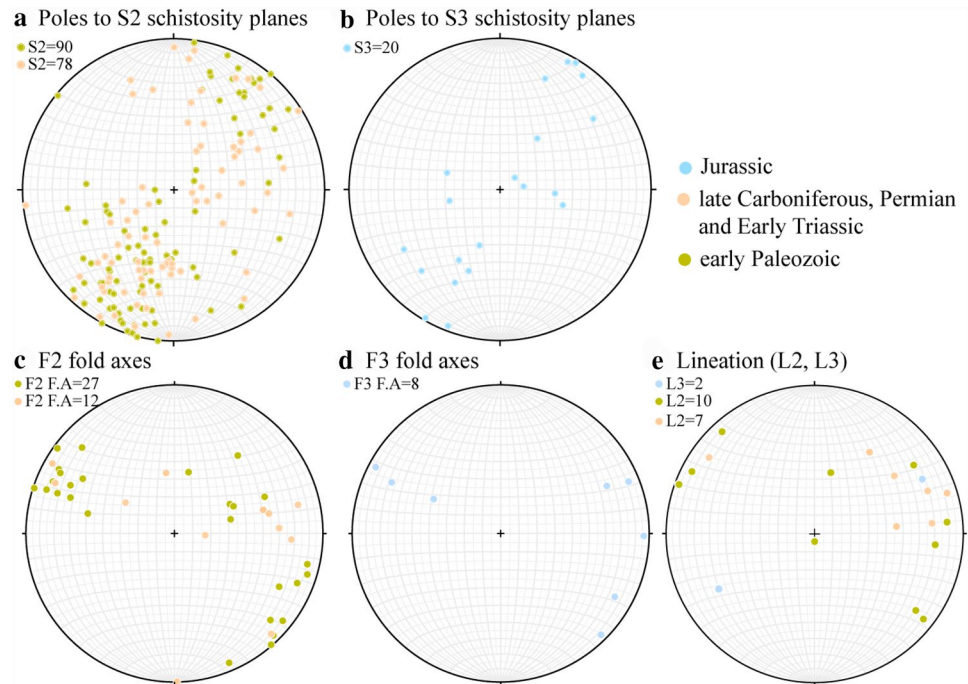


develops (S2), which forms the main schistosity of our study area (Fig. 6e).

The second of the two major folding phases shows more open, upright, parallel type of folds. These folds affect the Cretaceous units (K1; Fig. 5d) in addition to the older stratigraphic units, thus folding the S2 schistosity (Fig. 8a, d) and refolding the F2 folds (Fig. 5c). Therefore, these folds (F3) are younger than F2 and their age is post-Cretaceous. They show steeply dipping axial planes, which also strike WNW, as shown by the syncline of Dashte Pare Pire Anar (northern Gole Gohar area; Figs. 5e, 6f).

The outcrop pattern of tight to isoclinal, large-amplitude F2 folds is confirmed at the map scale, particularly in the northern part of the Qatruyeh area (Fig. 3), by the existence of several repetitions of early Paleozoic units (PZ3, PZ4; UNIT IV) which appear as elongate bands striking parallel to the general trend of the SSZ. A well-exposed, km-scale outcrop of such folds is located in the western Kuhe Ziyarat (Figs. 3, 4b, 5c), where late Carboniferous–early Permian layers (PC; UNIT IV) can be continuously observed from the thinned limbs to the thickened hinge of the F2 fold. F2 and F3 fold axes show similarly shallow WNW or ESE plunge (Fig. 7c, d). The refolded folds, as shown in Fig. 5c, correspond to Ramsay's Type 3 interference pattern.

## Fabric elements

The prevalent tectonic foliation (S2; Fig. 6d, e) strikes dominantly NW–SE and locally E–W (Fig. 7a). In the early Paleozoic (PZ, SD, Dm, DC sequences) and late Paleozoic to Permo-Triassic (PC, P, PTRd) units, the foliation planes mostly strike NW–SE and WNW–ESE (Figs. 3, 7a), and only in the northeastern most part of our study area, their main strike is oriented N–S (Fig. 7a; Permo-Carboniferous and Permo-Triassic units). Foliation planes in younger units, especially within the Jurassic ones, strike predominantly NW–SE and partly N–S (Fig. 7b). Due to folding of the main foliation, its dip direction varies from NE to SW, with the latter direction being dominant. In summary, the structural grain of all units strikes WNW-ESE, in spite of minor variations.

Elongate calcite and quartz grains define stretching lineations whose direction varies from NW–SE to NE–SW, and whose plunge is always shallow (Figs. 6a, 7e). The S2 foliation is defined by the preferred orientation of subparallel, thin, elongate biotite and flattened quartz grains in gneisses. In phyllites and low-grade schists, the S2 foliation is crenulated and the folded cleavage domains (phyllosilicates) define an S3 foliation (Fig. 8a, d). Such a foliation (S3) is exposed in the Kore Sefid and Qatruyeh areas.
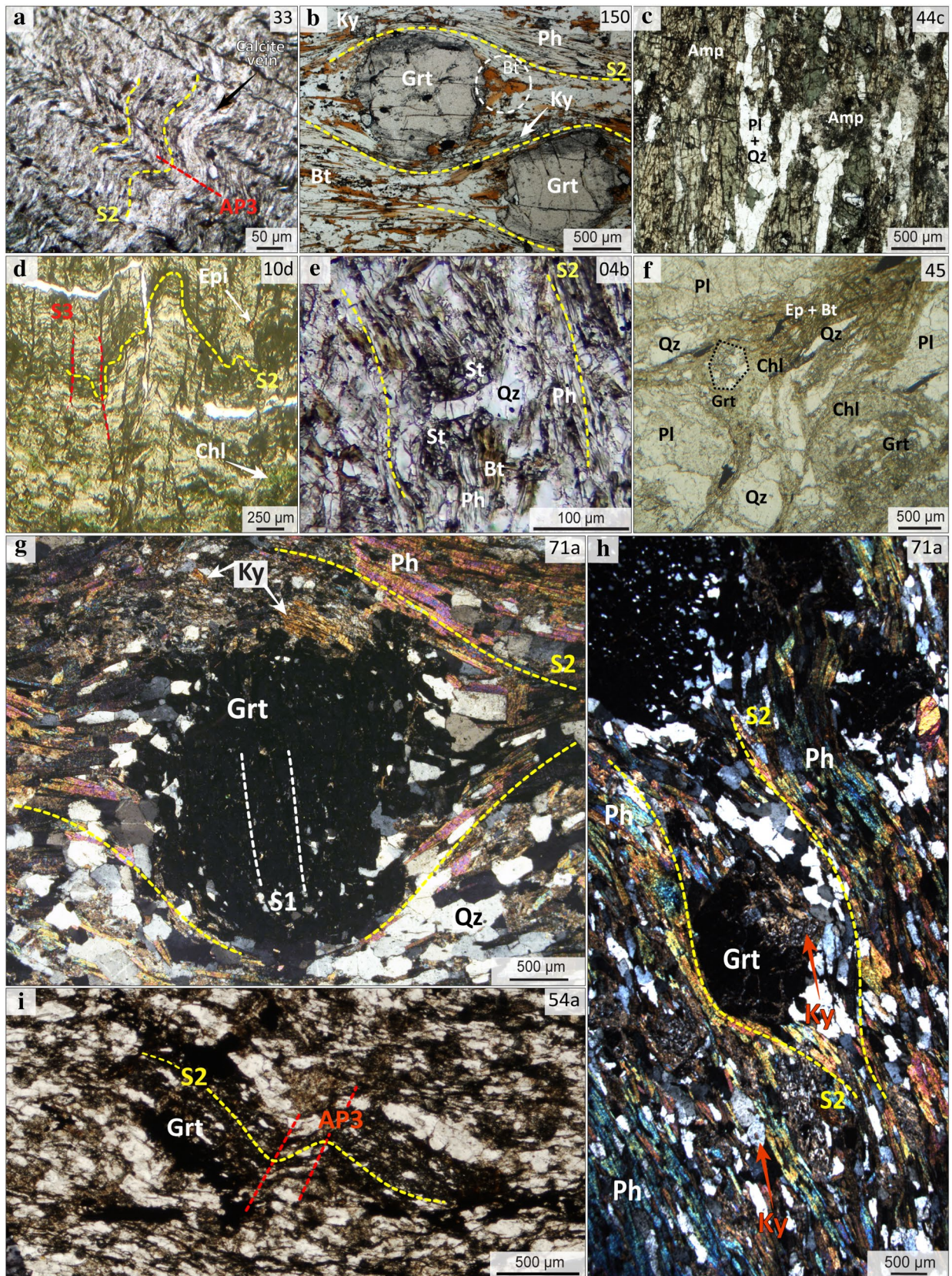
◀**Fig. 8** Photomicrographs of representative samples, **a** Foliation in phyllite from early Carboniferous of UNIT II in the Qatruyeh area. **b** High-T foliation showing the presence of kyanite within garnet strain caps (kyanite-bearing garnet micaschist; early Paleozoic unit of Kore Sefid area; UNIT IV). The yellow circle marks secondary biotites which are less deformed, more euhedral and partly cross-cut the pre-existence foliation. **c** Amphibolite grains showing a nematoblastic texture (pre-late Devonian from UNIT IV; southern Kore Sefid area). **d** Crenulation cleavage (S3, subvertical) in chlorite schist (early Carboniferous of UNIT IV; Gole Gohar area), developed by folded S2 (subhorizontal). **e** Staurolite porphyroblasts in garnet micaschist with S2 foliation that wraps around the staurolite overgrown by biotite grain (early Paleozoic of UNIT IV; Gole Gohar area). **f** Alteration of garnet and plagioclase to chlorite, sericite and clay minerals in retrogressed gneiss (pre-late Devonian of UNIT IV; southern Kore Sefid area). **g** Pre-tectonic (with respect to S2) garnet porphyroblast, showing pressure shadows with quartz, feldspar and strain caps, mainly consisting of phengite, within a kyanite-bearing garnet micaschist (early Paleozoic of UNIT IV; Sirjan region). Kyanite overgrowth on the outer rim of garnet, indicating its stability at peak metamorphic conditions. The trails of inclusions mark the previous schistosity (with respect to S2). **h** Sub-idiomorphic, pre-tectonic garnet (with respect to S2) wrapped by phengite, showing pressure shadows, which mainly consist of quartz grains. Retrograde growth of sericite is visible on the kyanite grain. **i** Post-tectonic garnets (post-D2) with elongated and folded quartz inclusions parallel to external foliation, replaced by secondary phases (mainly biotite and opaque phases). [Mineral abbreviations from Whitney and Evans 2010]

## Petrography of the studied samples

Samples, whose metamorphic conditions vary from amphibolite to greenschist facies, were collected from different lithologies (metagranites and metasedimentary rocks) along two cross sections, between the Neyriz and Sirjan regions (Fig. 3 and online resource 3). Samples used for petrological studies are not oriented and they include slates and phyllites (Fig. 8a), micaschists (Fig. 8b, g), amphibolites (Fig. 8c), gneisses (Fig. 8f), quartzites and metacarbonates. Mineral occurrences are given in Table 1 (abbreviations from Whitney and Evans 2010). Most studied samples consist of quartz + plagioclase + mica (biotite and muscovite) ± garnet ± kyanite ± staurolite in micaschists, and quartz + plagioclase + amphibole ± garnet in amphibolites. In two cases (samples 01* and 71b from the early Paleozoic sequences of Units II and IV respectively), garnet amphibolites also contain clinopyroxene (< 10 vol%; modal percentage based on Terry and Chilingar 1955).

The micaschists of the early Paleozoic and Precambrian formations commonly comprise biotite, muscovite, quartz, feldspar and garnet. Kyanite is present in some samples (Fig. 8b, g; samples 71a, 150 and 151). Sample 04b (Fig. 8e) from early Paleozoic rocks (PZ4; UNIT IV) contains very small staurolite grains (mostly ≤ 5 µm) together with kyanite and garnet. Intergrowths of staurolite and biotite advocate for the crossing of the reaction between garnet and chlorite. Some samples (e.g. sample 150) show sillimanite overgrowing muscovite (Fig. d of online resource 2). The foliation

(S2) in these early Paleozoic high-grade micaschists consists of mica-rich layers, including staurolite grains (Fig. 8e; PZ4 layers of UNIT IV) in rare cases and oriented mica flakes with kyanite (Fig. 8g; PZ2 layers of UNIT IV). The preferred orientation of mica domains results in a lepidoblastic texture (Fig. 8b, g, h; early Paleozoic sequences of UNIT IV). Some garnet grains, bordered by strain shadows and strain caps, are inferred to predate the S2 foliation (Figs. f of online resource 2 and 8g, h). In some cases these garnets are largely replaced by quartz and biotite grains (Fig. f of online resource 2) suggesting that they are not in equilibrium with respect to their surrounding S2 matrix, corroborating their pre-S2 growth. Some samples (e.g. sample 54a; UNIT IV) contain garnets with inclusion trails parallel to the external S2 foliation that point to post-S2 growth (Fig. 8i). Other garnet grains, with euhedral shape and no strain shadows nor deflection of the mica-rich matrix around them, overgrow the S2 schistosity (Fig. 9b). Hence, we interpret them as post-tectonic with respect to S2.

Except for some high-grade micaschists, the early Paleozoic units consist of lower grade metamorphic rocks, mainly phyllites (DC layers of UNIT III; Figs. 3, 8a) and low-grade schists (DC layers of UNIT IV; Figs. 3, 8d). The phyllites are fine-grained and they show foliation planes defined by the alternation of muscovite-rich and quartz-rich layers. In the low-grade schists, where muscovite and feldspar were altered to a mixture of chlorite, epidote, sericite and calcite, chlorite marks the S2 schistosity. S3 only developed within low grade conditions, and it consists of a crenulation cleavage characterized by phyllosilicate-rich domains (mainly chlorite) with some epidote grains (Fig. 8d).

A late greenschist facies overprint is observed in all samples. It is marked by the growth of chlorite and secondary biotite along cracks and rims of garnet grains and by the replacement of feldspar and kyanite by muscovite (Fig. 8b, h and Fig. c of online resource 2).

Figure 9a, b provides a summary of the relationships between mineral (over)growths, successive schistosities and deformation stages. In the following, we focus on the mineral chemistry of the micaschist samples used to determine the P–T metamorphic conditions (samples 71a, 150; early Paleozoic rocks from UNIT IV).

## Whole-rock and mineral chemistry

Whole-rock compositions of the samples used for thermodynamic modelling (71a and 150; UNIT IV) were estimated via chemical mapping of the polished thin sections using a scanning electron microscope (SEM) at CAMPARIS (Sorbonne Université, France). Electron probe microanalyses were carried out at CAMPARIS using a Cameca SX-100. Point analyses were performed using a 15-kV acceleration

**Table 1** Paragenesis of some representative samples with corresponding GPS coordinates

| Area | Sample | Grt | Bt | Ms | Amp | Ky | Sil | St | Accessory | Latitude | Longitude | Rock type | Stratigraphic age[a] |
|---|---|---|---|---|---|---|---|---|---|---|---|---|---|
| Seh Qalatun | 01* | * | * | | * | | | | Ms, Ap, Ep, Opq | 29.401 | 54.448 | Grt Amphibolite | PZ4 |
| | 03* | * | * | | | | | | Ms, Ap, Opq | 29.404 | 54.458 | Grt Bt Schist | PZ3 |
| | 05* | | | | * | | | | Ms, Ep | 29.425 | 54.459 | Amphibolite | PZ3 |
| Kore Sefid | 09* | * | * | * | | | | | Chl, Ms, Ap, Opq, Tur | 29.560 | 54.589 | Grt Micaschist | Dc.a |
| | 10* | * | * | * | | | | | Chl, Ms, Ilm | 29.570 | 54.590 | Grt Micaschist | Dc.a |
| | 11* | * | * | | | | | | Ms, Ep | 29.571 | 54.604 | Deformed granite | SD |
| | 13* | * | * | * | | | | | Ms, Tur | 29.552 | 54.590 | Grt Micaschist | Dc.a |
| | 08* | * | * | * | | | | | Chl, Ms, Ap, Graphite | 29.536 | 54.615 | Grt Micaschist | Dc.a |
| | 50 | | * | * | | | * | | Ms, Ep, Opq | 29.515 | 54.529 | High Silica Micaschist | SD |
| | 53a | | * | | | | * | | Ms, Opq | 29.537 | 54.571 | Bt Schist | Dd.s |
| | 52b | * | * | * | | | | | Chl, Ms, Ep | 29.530 | 54.558 | Orthogneiss with Grt | Dd.s |
| | 46c | * | * | * | | | | | Ms, Ilm | 29.541 | 54.647 | Grt Micaschist | Dc.a |
| | 44b | * | * | * | | | | | Ms, Opq | 29.508 | 54.661 | Bt schist with Grt | Dd.s |
| | 44c | | | | * | | | | Ms, Opq, Spn | 29.500 | 54.65 | Amphibolite | SD |
| | 45 | * | * | * | | | | | Ms, Ep, Opq | 29.511 | 54.652 | Orthogneiss | SD |
| | 149 | * | * | * | | | | | Chl, Ms, Tur, Opq | 54.353 | 29.335 | Grt Micaschist | SD |
| | 150 | * | * | * | | * | * | | Chl, Ms, Opq, Ilm, Tur | | | Grt Micaschist with Ky | SD |
| | 151 | * | * | * | | * | | | Chl, Ms, Tur, Opq, Ilm | | | Grt Micaschist with Ky | SD |
| Qatruyeh | 06b* | * | * | | * | | | | Ms, Zrn, Ap, Opq | 29.435 | 54.529 | Grt Bt Schist with Amp | PZ3 |
| | 07c* | * | * | * | | | | | Chl, Ms | 29.430 | 54.537 | Grt Ms schist | PZ4 |
| | 54a | * | | * | | | | | Ms, Opq, Cal | 29.465 | 54.597 | Grt Ms Schist | J1f[b] |
| | 38 | | | * | | | * | | Ms, Opq, Cal | 29.393 | 54.710 | Schist | J1f[b] |
| | 67 | | * | * | | | | | Opq, Cal | 29.405 | 54.769 | High Silica Micaschist | J1f |
| | 33 | | | * | | | | | Opq, Cal | 29.357 | 54.643 | Phyllite | DC |
| | 32c | | * | * | | | | | Ep, Opq, Cal | 29.270 | 54.669 | Phyllite | Pe |
| | 32a | | | | * | | | | Ep, Opq, Cal | 29.269 | 54.668 | Amphibolite | Pe |
| Gole Gohar | 02 | | * | | | | | | Ep, Opq | 29.270 | 55.045 | Bt Chl Schist | PZ3 |
| | 63a | | | * | * | | | | Ms, Opq, Cal | 29.269 | 55.043 | Amphibolite | PZ2 |
| | 63e | | | * | * | | | | Ms, Opq, Cal | 29.268 | 55.043 | Amphibolite | PZ2 |
| | 04b | * | * | * | | * | * | * | Ms, Tur, Opq | 29.172 | 55.033 | Grt Micaschist with St and Ky | PZ4 |
| | 05 | * | | * | | | | | Opq | 29.297 | 55.070 | Grt Ms Schist | PZ4 |
| | 10d | | | * | | | | | Ep, Cal | 29.308 | 55.102 | Chl Schist | DC |
| | 72 | * | * | * | | | | | Chl, Opq | 29.060 | 55.150 | Grt Micaschist | PZ4 |

**Table 1** (continued)

| Area | Sample | Grt | Bt | Ms | Amp | Ky | Sil | St | Accessory | Latitude | Longitude | Rock type | Stratigraphic age[a] |
|---|---|---|---|---|---|---|---|---|---|---|---|---|---|
| Sirjan | 60 | | | * | | | | | Cal | 29.258 | 55.620 | High Silica Ms Schist | PZ4 |
| | 61a | | * | | | | | | Ms, Opq | 29.243 | 55.639 | Granite mylonite | PZ4 |
| | 70c | | | | * | | | | Ms, Opq | 29.468 | 55.860 | Amphibolite | PZ3 |
| | 70d | * | * | * | | | | | Chl, Ms, Opq | 29.468 | 55.860 | Grt Micaschist | PZ3 |
| | 71a | * | * | * | | * | | | Chl, Ms, Ep, Tur, Opq, Rt | 29.452 | 55.836 | Grt Micaschist with Ky | PZ2 |

Sample localities are shown in Fig. 3. [Mineral abbreviation from Whitney and Evans 2010]

Stratigraphic ages: *Pe* Precambrian, *PZ2-4* early Paleozoic, *SD* pre-late Devonian, Dd.s, *Dc.a* pre-late Devonian-late Devonian, *DC* early Carboniferous, *JIf* Jurassic

[a]Stratigraphic ages are based on the geological maps

[b]Samples were taken from Jurassic units which are attributed to Paleozoic
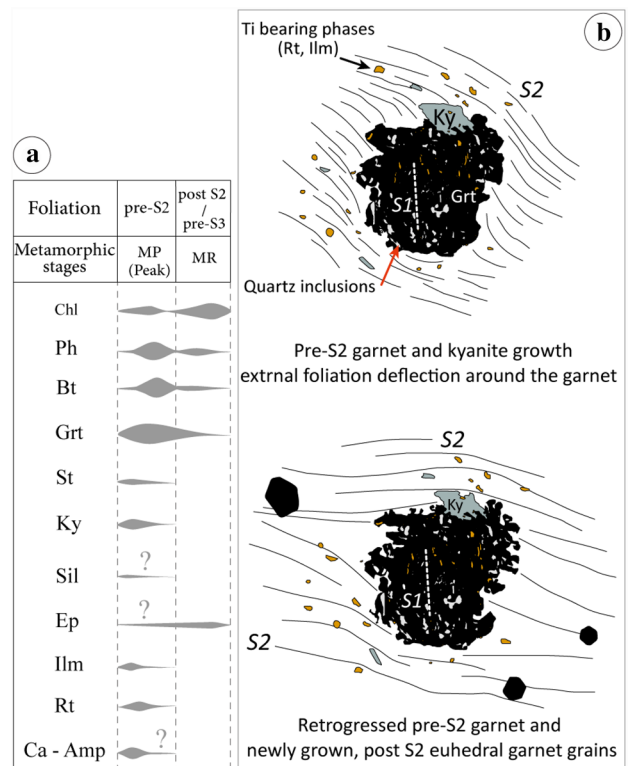


**Fig. 9 a** Inferred time of mineral growth with respect to fabric formation and metamorphic events. The relative thickness of the gray shadings indicates the abundance of minerals. *MP* prograde metamorphism (amphibolite facies). *MR* retrograde metamorphism (greenschist facies). Question mark indicates possible phase growth. **b** Schematic sketch showing garnet growth and the development of microstructures in its surrounding matrix through the major tectonic events that affected the southern SSZ. [Mineral abbreviations from Whitney and Evans 2010]

voltage, 10 nA beam current, ~3 μm beam size and wavelength dispersive spectroscopy (WDS) mode. Diopside (Ca, Mg, Si), $MnTiO_3$ (Mn, Ti), Orthoclase (K, Al), $Fe_2O_3$ (Fe), Albite (Na) and $Cr_2O_3$ were used as standards for measuring element concentrations. Element maps were transformed into compositional maps using the XMAPTOOLS software (Lanari et al. 2014; version 3.4.1, updated in 2019). The mineral formula was calculated using the software AX (Holland and Powell 2000; https://filedn.com/lU1GlyFhv3UuXg5E9dbnWFF/TJBHpages/ax.html), and the number of oxygen for this calculation is given in Table 2. Through the calculation by AX, the amount of ferric iron is calculated from stoichiometric constraints.

## Garnet

Garnets of analyzed samples (samples 71a and 150; UNIT IV; online resource 4) are almandine-rich ($Alm_{\sim60-70}$). The garnet grain of sample 71a consists of almandine (64–69 mol%), pyrope (9–21 mol%), and

**Table 2** Mineral compositions derived from EPMA analyses used to estimate the pressure and temperature by Perple-X pseudosection modelling and average P–T by THERMOCALC

| Sample no | 71a | | | | | | | | | 150 | | | | | | | | | 08* | 149 | 03* | 01* | 46 | 07c* |
|---|---|---|---|---|---|---|---|---|---|---|---|---|---|---|---|---|---|---|---|---|---|---|---|---|
| Phase | Grt C | Grt M1 | Grt M2 | Grt M3 | Grt R | Ph in matrix | Bt in matrix | Pl in matrix | Chl in matrix | Grt C | Grt M1 | Grt M2 | Grt M3 | Grt R | Ph in matrix | Bt in matrix | Pl in matrix | Chl in matrix | Ph | Grt | Bt | Amp | Pl | Grt |
| $SiO_2$ | 37.24 | 37.35 | 38.11 | 37.85 | 38.16 | 46.6 | 33.64 | 58.72 | 30.76 | 37.35 | 37.44 | 37.82 | 38.14 | 37.62 | 47.12 | 36.37 | 60.17 | 23.36 | 46.48 | 37.48 | 35.15 | 43.52 | 61.13 | 36.99 |
| $TiO_2$ | 0.02 | 0.92 | 0.02 | 0 | 0.06 | 0.79 | 1.24 | 0.02 | 1.09 | 0.10 | 0.06 | 0.08 | 0.05 | 0 | 1.06 | 1.68 | 0.02 | 0.08 | 0.34 | 0.04 | 2.93 | 1.27 | 0.03 | 0.05 |
| $Al_2O_3$ | 21.77 | 21.33 | 21.50 | 21.88 | 22.13 | 34.23 | 19.51 | 27.95 | 19.48 | 21.09 | 21.10 | 21.54 | 21.85 | 21.44 | 36.18 | 19.77 | 26.48 | 20.67 | 33.7 | 21.61 | 17.51 | 14.77 | 24 | 21.06 |
| $Cr_2O_3$ | 0.03 | 0.03 | 0.05 | 0 | 0.06 | 0.07 | 0 | 0 | 0.01 | 0.01 | 0.02 | 0.01 | 0 | 0.02 | 0 | 0.04 | 0 | 0 | 0.05 | 0.02 | 0.04 | 0.12 | 0.01 | 0.05 |
| $Fe_2O_3$ | 1.98 | 0.28 | 1.61 | 2.11 | 1.95 | 0.8 | 3.54 | 0.13 | 0 | 1.15 | 0.77 | 0.54 | 0.95 | 1.05 | 0.12 | 0 | 0.09 | 0 | 1.46 | 0.68 | 0 | 2.81 | 0.01 | 1.77 |
| $FeO$ | 28.36 | 30.27 | 30.81 | 30.49 | 31.37 | 1.53 | 18.05 | 0 | 22.55 | 28.02 | 29.25 | 30.65 | 31.80 | 31.90 | 1.11 | 17.61 | 0 | 29.62 | 1.46 | 30.14 | 18.44 | 11.33 | 0 | 31 |
| $MnO$ | 5.28 | 4.18 | 2.06 | 1.50 | 1.06 | 0 | 0.19 | 0.04 | 0.15 | 6.33 | 3.85 | 2.31 | 0.60 | 0.55 | 0.01 | 0.03 | 0.02 | 0.33 | 0 | 2.69 | 0.05 | 0.17 | 0.01 | 2.54 |
| $MgO$ | 2.39 | 2.96 | 4.30 | 4.78 | 4.98 | 1.14 | 12.76 | 0.01 | 13.23 | 1.28 | 1.91 | 2.46 | 3.82 | 3.90 | 0.85 | 10.49 | 0 | 9.61 | 1.41 | 4.48 | 9.88 | 11.07 | 0.01 | 4.58 |
| $CaO$ | 5.13 | 4.35 | 3.89 | 3.58 | 3.40 | 0 | 0.02 | 7.37 | 0.05 | 6.09 | 6.33 | 6.12 | 4.77 | 3.89 | 0.02 | 0 | 7.23 | 0.04 | 0.01 | 2.98 | 0.04 | 11.19 | 4.96 | 1.98 |
| $Na_2O$ | 0 | 0.03 | 0.01 | 0.03 | 0.00 | 1.26 | 0.29 | 7.97 | 0.06 | 0.05 | 0.02 | 0.02 | 0.05 | 0.09 | 0.8 | 0.26 | 7.68 | 0.05 | 0.98 | 0.03 | 0.23 | 1.5 | 8.99 | 0 |
| $K_2O$ | 0 | 0 | 0 | 0 | 0 | 8.9 | 5.38 | 0.05 | 4.07 | 0 | 0 | 0 | 0.03 | 0.06 | 9.23 | 8.09 | 0.07 | 0 | 9.96 | 0.02 | 9.22 | 0.93 | 0.08 | 0 |
| $O$ | 12 | 12 | 12 | 12 | 12 | 11 | 11 | 8 | 14 | 12 | 12 | 12 | 12 | 12 | 11 | 11 | 8 | 14 | 11 | 12 | 11 | 23 | 8 | 12 |
| $Si$ | 2.93 | 2.95 | 2.97 | 2.94 | 2.94 | 3.092 | 2.61 | 2.57 | 3.097 | 2.97 | 2.98 | 2.98 | 2.97 | 2.98 | 3.07 | 2.739 | 2.637 | 2.662 | 3.122 | 2.97 | 2.722 | 6.314 | 2.734 | 2.95 |
| $Ti$ | 0 | 0.06 | 0 | 0 | 0 | 0.039 | 0.072 | 0.001 | 0.083 | 0.01 | 0 | 0.01 | 0 | 0 | 0.052 | 0.095 | 0.001 | 0.007 | 0.017 | 0 | 0.171 | 0.139 | 0.001 | 0 |
| $Al$ | 2.02 | 1.98 | 1.97 | 2 | 2.01 | 2.677 | 1.78 | 1.442 | 2.313 | 1.98 | 1.98 | 2.00 | 2.01 | 2 | 2.779 | 1.755 | 1.368 | 2.777 | 2.668 | 2.02 | 1.598 | 2.526 | 1.266 | 1.98 |
| $Cr$ | 0 | 0 | 0 | 0 | 0 | 0.004 | 0 | 0 | 0.001 | 0 | 0 | 0 | 0 | 0 | 0 | 0.002 | 0 | 0 | 0.002 | 0.00 | 0.003 | 0.014 | 0 | 0 |
| $Fe^{+3}$ | 0.12 | 0.02 | 0.10 | 0.12 | 0.11 | 0 | 0 | 0 | 0.001 | 0.07 | 0.05 | 0.03 | 0.06 | 0.06 | 0.07 | 0 | 0 | 0 | 0 | 0.04 | 0 | 0.307 | 0 | 0.11 |
| $Fe^{+2}$ | 1.87 | 2.00 | 2.00 | 1.98 | 2.02 | 0.125 | 1.341 | 0 | 1.899 | 1.87 | 1.95 | 2.02 | 2.07 | 2.11 | 0.066 | 1.109 | 0 | 2.823 | 0.082 | 2.00 | 1.194 | 1.375 | 0 | 2.07 |
| $Mn$ | 0.35 | 0.28 | 0.14 | 0.10 | 0.07 | 0 | 0.012 | 0.002 | 0.013 | 0.43 | 0.26 | 0.15 | 0.04 | 0.04 | 0.001 | 0.002 | 0.001 | 0.032 | 0 | 0.18 | 0.003 | 0.021 | 0 | 0.17 |
| $Mg$ | 0.28 | 0.35 | 0.50 | 0.55 | 0.57 | 0.113 | 1.48 | 0.001 | 1.985 | 0.15 | 0.23 | 0.29 | 0.44 | 0.46 | 0.083 | 1.177 | 0 | 1.632 | 0.141 | 0.53 | 1.14 | 2.393 | 0.001 | 0.55 |
| $Ca$ | 0.43 | 0.37 | 0.32 | 0.30 | 0.28 | 0 | 0.001 | 0.346 | 0.005 | 0.52 | 0.54 | 0.52 | 0.40 | 0.33 | 0.002 | 0 | 0.34 | 0.005 | 0.001 | 0.25 | 0.004 | 1.739 | 0.238 | 0.17 |
| $Na$ | 0 | 0.01 | 0 | 0.01 | 0 | 0.162 | 0.043 | 0.677 | 0.012 | 0.01 | 0 | 0 | 0.01 | 0.01 | 0.101 | 0.038 | 0.653 | 0.011 | 0.128 | 0.01 | 0.035 | 0.422 | 0.779 | 0 |
| $K$ | 0 | 0 | 0 | 0 | 0 | 0.753 | 0.533 | 0.003 | 0.523 | 0 | 0 | 0 | 0 | 0.01 | 0.767 | 0.777 | 0.004 | 0 | 0.854 | 0 | 0.911 | 0.172 | 0.005 | 0 |
| Total | 8 | 8 | 8 | 8 | 8 | 6.966 | 7.87 | 5.045 | 9.93 | 8 | 8 | 8 | 8 | 8 | 6.921 | 7.694 | 5.005 | 9.95 | 7.017 | 8 | 7.781 | 15.52 | 5.024 | 8 |
| $X_{Mg}$ | 0.123 | 0.148 | 0.192 | 0.208 | 0.211 | 0.474 | 0.524 | – | – | 0.072 | 0.103 | 0.124 | 0.171 | 0.175 | 0.557 | 0.51 | – | – | 0.63 | 0.21 | 0.49 | 0.63 | – | 0.21 |
| $X_{prp}$ | 0.096 | 0.117 | 0.169 | 0.188 | 0.194 | – | – | – | – | 0.051 | 0.077 | 0.097 | 0.149 | 0.156 | – | – | – | – | – | 0.179 | – | – | – | 0.18 |
| $X_{grs}$ | 0.147 | 0.123 | 0.108 | 0.102 | 0.095 | – | – | – | – | 0.175 | 0.181 | 0.174 | 0.136 | 0.112 | – | – | – | – | – | 0.086 | – | – | – | 0.06 |
| $X_{alm}$ | 0.638 | 0.667 | 0.676 | 0.676 | 0.687 | – | – | – | – | 0.630 | 0.654 | 0.678 | 0.702 | 0.718 | – | – | – | – | – | 0.675 | – | – | – | 0.70 |
| $X_{sps}$ | 0.119 | 0.093 | 0.047 | 0.034 | 0.024 | – | – | – | – | 0.145 | 0.087 | 0.050 | 0.014 | 0.014 | – | – | – | – | – | 0.061 | – | – | – | 0.06 |

Garnet grain sections are shown in Fig. 10b, c

$X_{prp} = Mg/(Mg+Fe^{+2}+Ca+Mn)$, $X_{grs} = Ca/(Mg+Fe^{+2}+Ca+Mn)$, $X_{alm} = Fe^{+2}/(Mg+Fe^{+2}+Ca+Mn)$, $X_{Mg(Bt,Wms)} = Mg/(Mg+Fe)$, $X_{Fe(Bt)} = Fe/(Mg+Fe)$

*C* Garnet Core, *M* Garnet mantle, *R* Garnet rim. Mineral abbreviations from Whitney and Evans (2010)
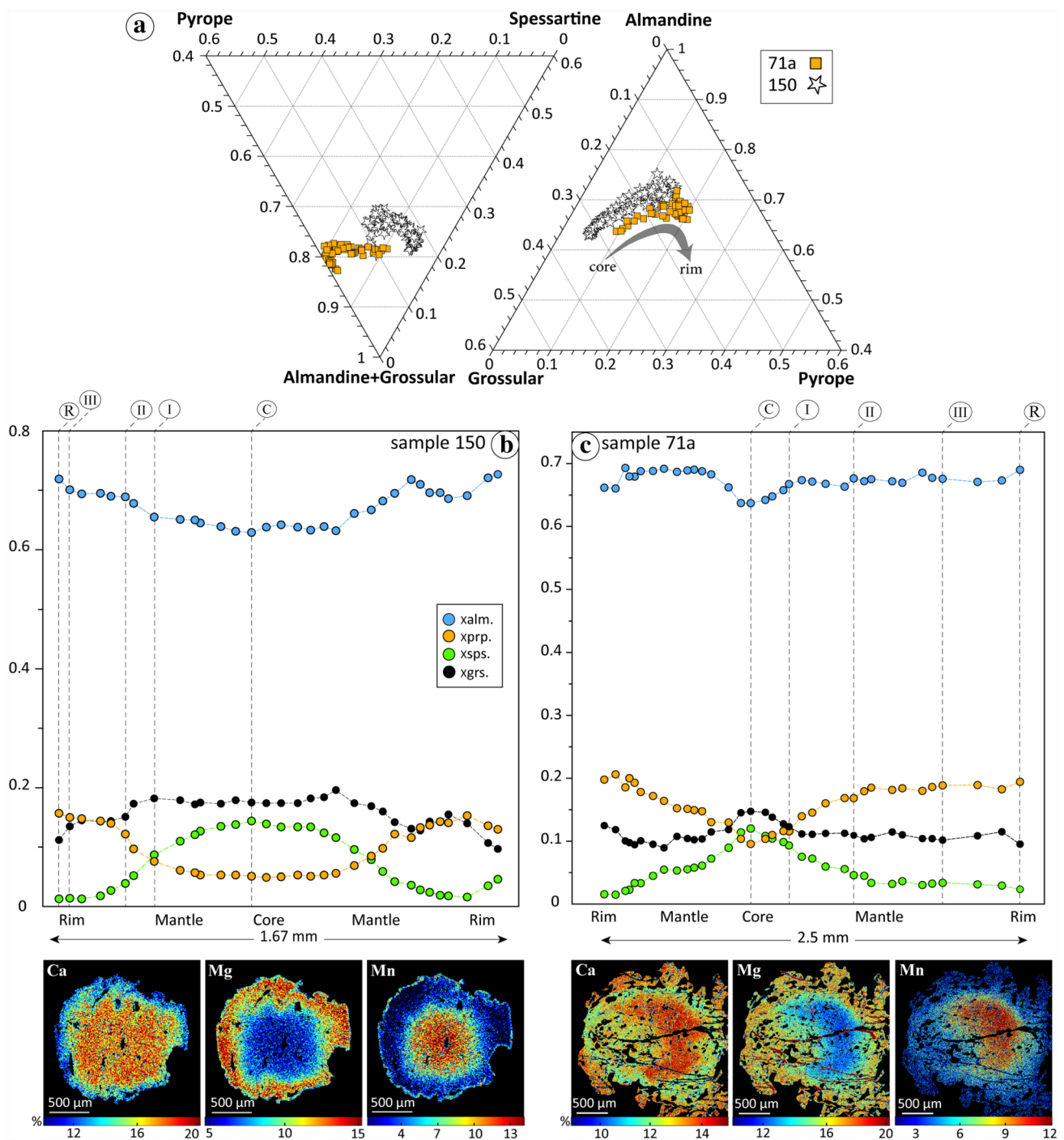
**Fig. 10** Chemical analyses of garnets. **a** Ternary diagrams showing the composition of analyzed garnets (compositional data from EPMA analyses are presented as online resource 4), **b**, **c** X-ray maps and chemical profiles of garnet grains obtained by EPMA from samples 150 and 71a. Abbreviations: *alm* almandine, *prp* pyrope, *sps* spessartine, *grs* grossular. On the garnet profile C, I–III and R refer to Core, Mantle and Rim of the analyzed garnet grains, respectively

grossular (9–15 mol%) components with minor spessartine (1–12 mol%). In comparison with sample 71a, the composition of garnet in sample 150 varies within a wider range (almandine: 63–73 mol%, pyrope: 5–16 mol%, grossular: 10–20 mol%, spessartine: 1–14 mol%). Compositional

profiles of representative garnet grains show a normal chemical zoning (Fig. 10a–c) marked by a core to rim decrease in Mn-content and increase in XMg ($Mg^{2+}/(Mg^{2+}+Fe^{2+})$). $X_{Mg}$ of garnet porphyroblasts increases from a minimum value
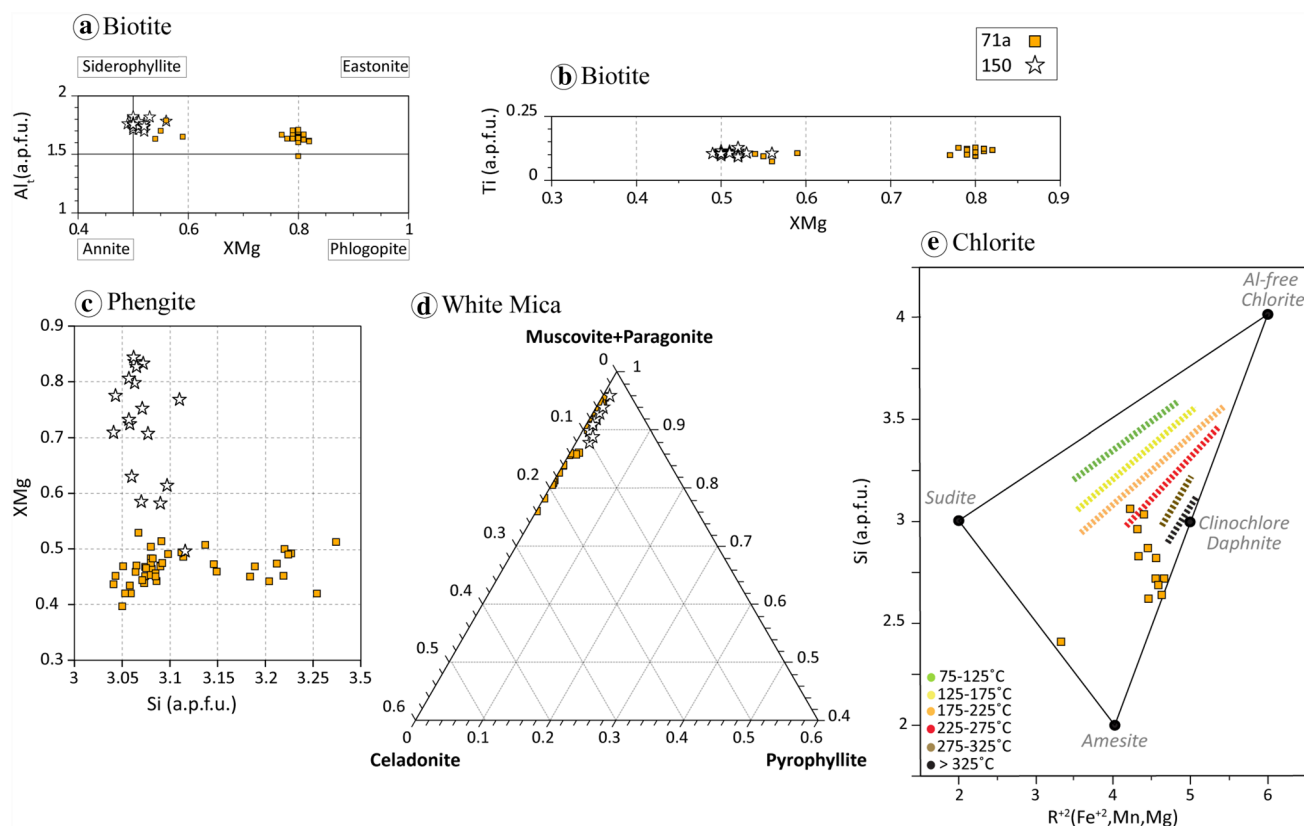
**Fig. 11** Compositional plots of minerals: **a**, **b** Biotite compositions plotted according to Al (total) and Ti (a.p.f.u.) versus XMg, **c** Phengite composition plotted as total Si based on a.p.f.u. versus XMg. **d** Ternary plot illustrating the composition of white mica. **e** Chlorite composition in the $R^{+2}$–Si diagram ($R^{+2}$ refers to divalent cations such as $Fe^{+2}$, Mn and Mg)

of ~ 0.13 (sample 71a) and ~ 0.08 (sample 150) in the core to ~ 0.22 (sample 71a) and ~ 0.18 (sample 150) at the rim.

## Biotite

In comparison to sample 150, biotite is significantly enriched in Mg in sample 71a (Fig. 11a) and closer to the phlogopite end-member (avg. XMg: ~ 0.54). In sample 150, the XMg of biotite varies in the range of 0.49–0.52 and is relatively close to the annite end-member (Fig. 11a). The tetrahedral Al content (Fig. 11a) is ~ 1.7–1.8 and ~ 1.4–1.7 a.p.f.u. in samples 150 and 71a, respectively. The maximum Ti content of biotite is around 0.1 a.p.f.u. for both samples 71a and 150 (Fig. 11b).

## White mica

The Si content of white mica ranges from 3.04 to 3.27 a.p.f.u. (Fig. 11c). The analyses indicate that mica plots along the muscovite–celadonite solid solution, most commonly close to the muscovite end-member composition (Fig. 11d). The paragonite content of white mica in samples

71a and 150 reaches ~ 10–20% and ~ 10%, respectively (Fig. a of online resource 5).

## Chlorite

Chlorite within our analyzed samples is mostly a secondary phase. Chlorite composition lies between amesite and clinochlore/daphnite (Fig. 11e; Bourdelle and Cathelineau 2015). The XMg and Si values for the garnet–kyanite-bearing sample (71a) are in the range of 0.39–0.52 and 2.61–3.29 a.p.f.u., respectively (Fig. b of online resource 5).

## P–T estimates

In order to determine peak metamorphic P–T conditions attained in the study area, pressure and temperature were estimated using the two representative samples of kyanite-bearing garnet micaschist from the early Paleozoic units of the Sirjan and Kore Sefid regions (samples 71a and 150; UNIT IV; Figs. 3, 8b and g). Both samples contain garnet porphyroblasts surrounded by a matrix consisting of muscovite and biotite flakes, quartz and plagioclase (mainly

andesine; Fig. c of online resource 5) in addition to ilmenite and rutile grains as accessory phases. Ilmenite is mostly included within garnet grains and rutile formed close to the garnet rims and in the matrix (online resource 6). In sample 71a, mica flakes are wrapped around rounded garnet porphyroblasts (Fig. 8g). Garnet is chemically zoned in both samples (Fig. 10), and contains inclusion trails of quartz, rutile and ilmenite (Figs. f of online resource 2 and Fig. 9b) in sample 71a. Quartz inclusions in garnets exist in different sizes and are distributed irregularly. The bigger grains of ilmenite and rutile developed in the marginal zone of the garnets that can indicate increasing pressure and temperature towards the rim. These rounded garnet grains were partially replaced by secondary biotite. Considering the existence of pressure shadows and strain caps, and their irregular, rounded boundaries, these grains belong to a garnet generation pre-dating S2. Kyanite grains are aligned in the penetrative S2 schistosity (Fig. 8b). They were mostly replaced by sericite in sample 71a, but they are fresher and almost unaltered in sample 150. In addition, some garnet grains with quartz inclusion parallel to the penetrative external schistosity (S2) are also present and illustrate post-S2 growth (Fig. 8i).

## Conventional and multi-equilibrium thermobarometry

Average P–T conditions for the Grt-Pl-Bt-Ms-Chl-Qz-bearing assemblages were estimated using the program THERMOCALC (version 3.33, with the June 2009 upgrade; Holland and Powell 1998, 2011). Assuming mineral equilibrium with garnet rims yields $674 \pm 24$ °C and $8.8 \pm 0.9$ kbar (Fig. 12a) for sample 71a (Fig. 8g shows the petrography of sample 71a) and $691 \pm 42$ °C and $7.9 \pm 1.5$ kbar (Fig. 12b) for sample 150 (Fig. 8b). These estimates are broadly consistent with the pressure estimated by GASP (Holdaway 2001), around 8 kbar for both samples, and with garnet–biotite thermometry for the garnet rims, with temperature estimates between 605 and 690 °C (considering a peak pressure of 8–9 kbar; sample 71a: 647–690 °C, sample 150: 605–633 °C). The average temperature for sample 71a (668 °C) is ~50 °C higher than for sample 150. This difference is in line with temperature estimates derived from the Ti-content of biotite (Holdaway 2000; Henry et al. 2005), which are in the range 667–691 °C and 597–621 °C for samples 71a and 150, respectively.

## Thermodynamic modelling

Thermodynamic modelling was performed for samples 71a and 150 in the system MnO–Na$_2$O–CaO–K$_2$O–FeO–MgO–Al$_2$O$_3$–SiO$_2$–H$_2$O–TiO$_2$ (MnNCKFMASHT) with the Perple-X software (Connolly 2005). The location of the calculate

d garnet isopleths (X$_{Ca}$ and X$_{Mg}$; Table 2) was compared to compositions derived from EPMA data to refine the P–T evolution of the samples. Calculations were performed with Perple-X version 6.8.6 (hp04ver database; Holland and Powell 1998).

Solution models considered for garnet, biotite, phengite, chloritoid, staurolite, chlorite, epidote and melt are the HP models of Holland and Powell (1998) and Holland et al. (1998), with feldspar (Newton et al. 1980) and IlGkPy for Mn-bearing ilmenite. Changes in bulk composition as a result of garnet growth zoning were neglected due to the small amount (< 10 vol%) of modal garnet in the samples. Given the abundance of phyllosilicates, and in particular phengite, calculations were performed with excess water. Since micaschists contain apatite, P$_2$O$_5$ was omitted because its contents in the major silicate minerals are negligible. Considering the absence of Fe$^{+3}$-rich phases such as magnetite in the studied samples, Fe$_2$O$_3$ was neglected. The P–T conditions for the onset of core growth, mantle and rim development are estimated using the intersections between the garnet compositional isopleths X$_{Ca}$ and X$_{Mg}$; Fig. 12a, b and Table 2) for each respective garnet zone (C, I, II, III and R; with ~5% of uncertainties on the EPMA analyses; Lifshin and Gauvin 2001). With increasing pressure and temperature, the X$_{Ca}$ and X$_{Mg}$ of garnet increase in both samples (Fig. 12). In addition to the garnet isopleths, the Si content of phengite is used to refine the pressure conditions.

The intersections of compositional isopleths of garnet cores point to the onset of garnet growth under mid-amphibolite facies conditions (71a: ~7kbar, ~570 °C; 150: ~6 kbar, ~540 °C; stage C in Fig. 12a, b). Garnet growth in sample 71a occurred outside of the biotite stability field, in the presence of plagioclase and chlorite (stage C in Fig. 12a) whereas it began in the phengite+feldspar+biotite+chlorite+ilmenite field (labeled C on Fig. 12b) under lower pressure in sample 150. The prograde path recorded by garnet growth in sample 71a continued in the absence of biotite where phengite, chlorite and plagioclase still coexist (stage I in Fig. 12a), and garnet growth in sample 150 developed inside the chlorite and biotite stability fields (stages C to I and II; Fig. 12b). Garnet growth continued along an up-pressure path across the biotite+phengite+plagioclase±chlorite±rutile±staurolite±kyanite field, reaching peak pressure just past the chlorite-out reactions in the phengite+feldspar+biotite+garnet+rutile±kyanite field (labeled II-R on Fig. 12a, b). Garnet and kyanite appear with P–T increasing, growing at the expense of staurolite. The garnet–biotite–kyanite–plagioclase–phengite–rutile bearing mineral assemblage of sample 71a suggests peak burial conditions of ~9 kbar and 655 °C (Fig. 12a). Core to mantle (C-III) compositions suggest that pressure and temperature increased from 7.5 to 9 kbar and ~570 to 640 °C (Fig. 12a). Pseudosections suggest that kyanite is part of the peak mineral assemblage for sample 71a and appears during the early decompression
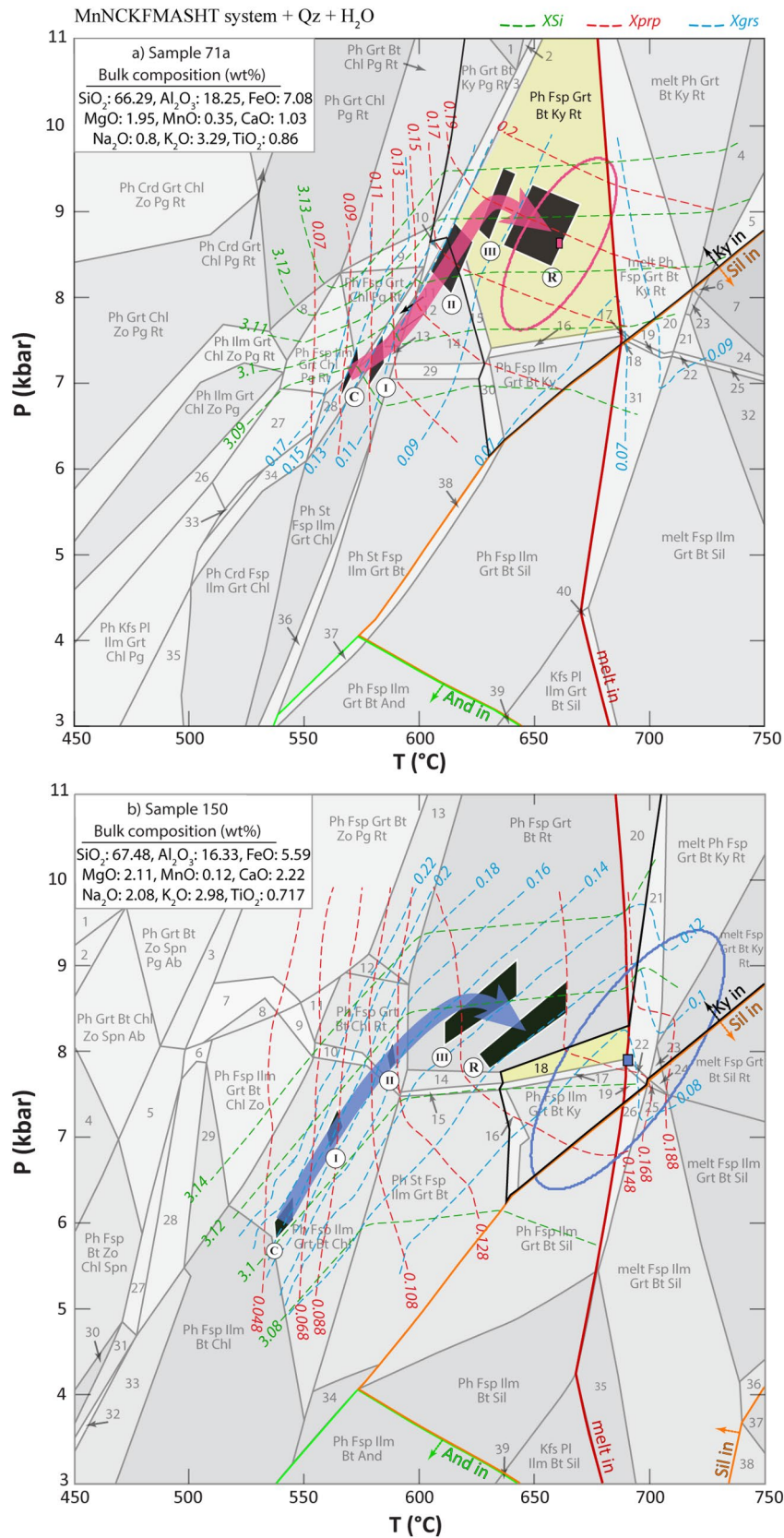
◄**Fig. 12** Pseudosections (MnNCKFMASHT system) constrained for kyanite garnet micaschist: **a** Sample 71a, **b** Sample 150. Black fields illustrate the intersection of garnet isopleths (Xprp and Xgrs) considering 5% of uncertainty. They are labeled as C, I–III and R refer to Core, Mantle and Rim of analyzed garnet grains. All fields of pseudisection contain quartz and excess $H_2O$. Field legend: **a** 1: Ph Grt Bt Pg Rt, 2: field1+Fsp, 3: field1+Fsp+Ky, 4: melt Ph Grt Bt Ky Rt-$H_2O$, 5: field4-Ph, 6: field4-Ky+Sil, 7: melt Grt Bt Sil Rt-$H_2O$, 8: Ph Ilm Grt Chl Pg Rt, 9: field8+Fsp+Bt, 10: Ph St Fsp Grt Bt Pg Rt, 11: field10-Bt+Chl, 12: Ph St Fsp Grt Chl Rt, 13: field12+Ilm, 14: field12-Chl+Bt, 15: Ph St Fsp Grt Bt Ky Rt, 16: field15-St+Ilm, 17: melt Ph Fsp Ilm Grt Bt Ky Rt, 18: field17-Rt, 19: field17-Ky+Sil, 20: melt Ph Fsp Grt Bt Sil Rt, 21: field20-Ph, 22: field20-Ph+Ilm, 23: melt Ph Fsp Grt Bt Sil Rt-$H_2O$, 24: field23-Ph, 25: field23-Ph+Ilm, 26: Ph Fsp Ilm Grt Chl Zo Pg, 27: Ph Fsp Ilm Grt Chl Pg Mag, 28: field27+St-Mag, 29: Ph St Fsp Ilm Grt Bt Rt, 30: Ph St Fsp Ilm Grt Bt Ky, 31: field19-Rt, 32: melt Fsp Ilm Grt Bt Sil-$H_2O$, 33: Ph Crd Fsp Ilm Grt Chl Pg Mag, 34: field33-Mag, 35: field33-Pg-Mag, 36: field29-Rt+Chl, 37: field29-Rt+And, 38: Ph St Fsp Ilm Bt Sil, 39: Kfs Pl Ilm Grt Bt And, 40: melt Kfs Pl Ilm Grt Bt Sil. **b** 1: Ph Grt Chl Zo Spn Pg Ab, 2: field1-Pg, 3: Ph Fsp Grt Bt Zo Spn Pg, 4: Ph Bt Chl Zo Spn Ab, 5: field3-Pg+Chl, 6: field3+Chl, 7: Ph Fsp Ilm Grt Bt Zo Pg Rt, 8: field3-Spn+Ilm, 9: Ph Fsp Ilm Grt Bt Chl Zo Pg, 10: Ph Fsp Ilm Grt Bt Chl Rt, 11: Ph Fsp Grt Bt Chl Zo Rt, 12: field11-Zo+Pg, 13: Ph Fsp Grt Bt Pg Rt, 14: field13-Pg+St, 15: Ph St Fsp Ilm Grt Bt Rt, 16: field15-Rt+Ky, 17: field15-St+Ky, 18: Ph Fsp Grt Bt Ky Rt, 19: melt Ph Fsp Ilm Grt Bt Ky, 20: melt Ph Fsp Grt Bt Rt, 21: field20+Ky, 22: field20+Ilm+Ky, 23: melt Fsp Grt Bt Ky Rt, 24: field23-Ky+Sil, 25: melt Fsp Ilm Grt Bt Sil Rt, 26: field25-Ph-Rt, 27: Ph Fsp Ilm Bt Chl Zo Spn, 28: field27-Spn+Rt, 29: field27-Spn, 30: field-Ilm-Zo, 31: field27-Zo, 32: field27-Zo+Rt, 33: Ph Fsp Ilm Bt Chl, 34: Ph St Fsp Ilm Bt, 35: melt Fsp Ilm Bt Sil, 36: melt Fsp Ilm Grt Bt Sil Crd Qz-$H_2O$, 37: field36-Sil, 38: melt Fsp Ilm Grt Bt Crd, 39: Fsp Ilm Bt And [Abbreviation from Whitney and Evans 2010]

stage for sample 150 (Fig. 12). Increasing temperature from mantle to rim of the garnet grains (~630 to ~640 °C) accompanied with decompression (sample 71a: 9–7.9 kbar, sample 150: 8.5–~8 kbar) implies a clockwise P–T path after peak metamorphism.

Peak burial conditions are roughly similar for samples 150 and 71a, though somewhat higher for sample 71a (Fig. 12b). This is consistent with average P–T estimates for sample 71a (8.8±0.9 kbar, 674±24 °C) and 150 (7.9±1.5 kbar, 691±42 °C). The Si content of phengite ranges between 3.04 and 3.11 a.p.f.u. in sample 150, consistent with the area defined by index minerals and garnet isopleths (Fig. 12b). The wider range of Si contents for sample 71a varies (3.04–3.27 a.p.f.u.) suggests that some phengite formed at higher P–T conditions and that peak pressure conditions deduced here should be regarded as a lower bound.

## Discussion

### Tectono-metamorphic evolution

The structural analysis combined with our petrological results indicates that the southern SSZ has been affected by polyphase deformation (D1, D2, D3) and metamorphism (prograde and retrograde). Structures related to D1 (Fig. b of online resource 2) are only rarely observed, most probably because it was strongly overprinted by D2, which shows the same style of deformation. Indeed, D2 is characterized by tight to isoclinal F2 folds (e.g. UNITs II, III; Fig. 13); thus the overprint of previous phases was intense. These F2 folds are associated with the pervasive S2 foliation described above, which wraps around the garnets grains, whose rims define the metamorphic peak conditions (Sect. 6.1). Hence, D2 developed after the peak of amphibolite-facies metamorphism. The precise temperature conditions of the D2 event are not constrained, but it appears to have taken place under greenschist-facies conditions, in the stability field of biotite (Fig. 8b). Sheikholeslami et al. (2008) assessed that the main schistosity of the southern SSZ consists of a syn-metamorphic, composite S1+S2 foliation. Our observations are consistent with the latter interpretation and they suggest that amphibolite facies metamorphism precedes D2, hence being possibly associated to S1. Only at the thin-section scale, the presence of preserved foliations at high angle to S2 within microlithons (Fig. c of online resource 2) and the trails of inclusions in some garnet grains (Fig. h of online resource 2) point to the existence of a pre-S2 schistosity, possibly contemporaneous to garnet growth. It is likely that this pre-S2 schistosity corresponds to the local occurrence of S1 described above.

Based on the existence of an angular unconformity between the early Paleozoic and Jurassic sequences, and on the absence of unconformity between the Permian and the Carboniferous, these events were attributed to the early Cimmerian orogeny (Sheikholeslami et al. 2008). Sheikholeslami (2015) suggested that two major tectono-metamorphic events affected the southern SSZ: the first one, concluded to be Late Triassic–Early Jurassic, was coeval with amphibolite facies metamorphism, and it resulted in four successive folding phases, and three distinct schistosities. Our observations also suggest that the main foliation is a composite (S1+S2), although we do not observe four distinct fabric elements. This foliation and its associated F2 folds, which post-date the high-temperature Barrovian metamorphism (Fig. 12). Sheikholeslami et al. (2008) also described a non-penetrative, late-Cimmerian deformation phase, affecting the overlying Cretaceous limestones. Field observations of the present
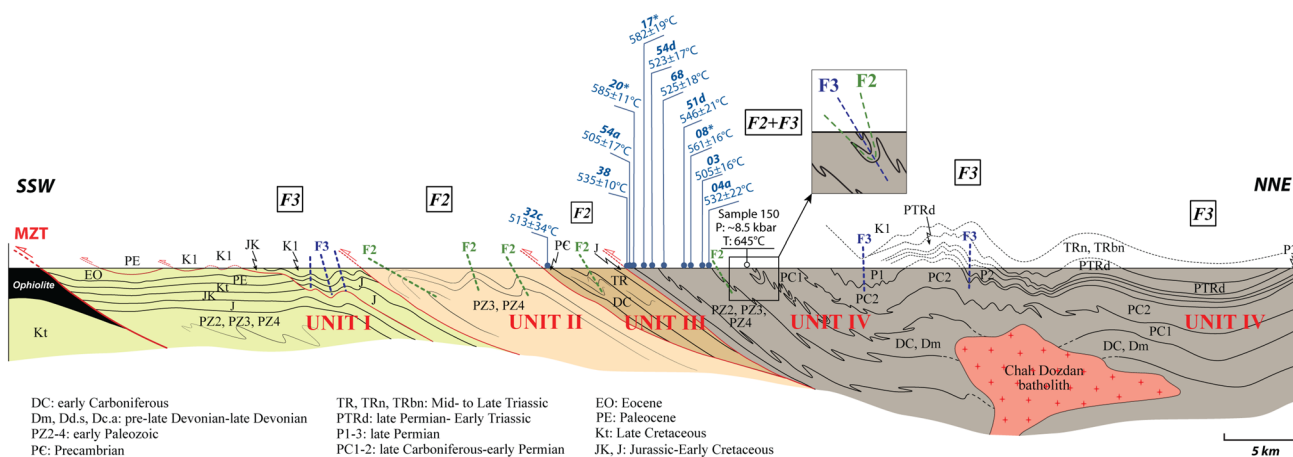
**Fig. 13** Synthetic cross-section of the southern SSZ. Note the presence of four major tectonic units, as described in the text. The locations of sample 150 and the peak temperatures obtained by Raman (Gharibnejad et al. 2020) are illustrated. The section is constructed by lateral projection of tectonic and lithological contacts based on sections of Fig. 4. The green and blue dashed lines display the trace of F2 and F3 axial planes

study indicate that the D3 phase, developed open, upright folds (F3; Fig. 5e), which overprinted the D2 structures (UNIT IV; Fig. 13). This episode affected all units including Cretaceous (Figs. 5e and 13), partly refolding F2 structures (Figs. 5c, 13; UNIT IV). We observed no evidence of syn-D3 metamorphism, except for very local, very low-temperature foliations, partly related to folds and partly to localized shear planes (Fig. 8a, d). Therefore, greenschist facies overprinting of the high-temperature assemblages must have preceded D3. Sheikholeslami et al. (2008) recognized a late, post-metamorphic S3 foliation that is associated with a post-Triassic folding event with fold axes oriented NW–SE. They subdivided this second tectono-metamorphic event into three folding phases, which generated two distinct greenschist-facies schistosities, inferred to have formed during Late Jurassic times and continuous subduction of the Neotethys (Sheikholeslami 2015). Our observations described above are more consistent with the attribution of the S3 schistosity and its associated F3 folding to post-Cretaceous time, instead of Jurassic, with shortening being due to closure of the Neotethys and/or collision along the Zagros Belt.

In addition to the dominant D2 structures, our study area is structured by a sequence of four major, gently ENE dipping tectonic units (Figs. 3 and 4). As best exemplified by the uppermost of these units, they cut across basement and cover rocks, bounding distinct tectonic units, which include metamorphic rocks of very different temperatures. As a consequence, the basal thrusts of these units are post-metamorphic, hence post-D2. We suggest that these thrusts are roughly synchronous to the D3 folding event, hence post-Cretaceous.

Field observations and structural data collected in the present study are not consistent with the many distinct schistosities described by previous studies (Sheikholeslami et al. 2008; Sheikholeslami 2015). We can only reliably assess the occurrence of one main schistosity (S2) that is associated with large-scale tight- to isoclinal folds (F2) in addition to an older (S1) and a younger (S3) schistosities that are only locally present.

Rising of diapiric gneiss in Triassic time (early Cimmerian) was suggested to explain the exhumation of the high-temperature metamorphic rocks of the southern SSZ (Sheikholeslami et al. 2008). They suggested that the diapiric domes are bounded by divergent folds on their sides and that no detachment faults juxtapose the low- and high-grade metamorphic rocks. Our observations and interpretations, as documented in the cross sections of Fig. 4 are incompatible with diapiric geometries. In addition, only small areas are characterized by partial melting, which could provide the necessary conditions for a diapiric rise are exposed. However, a sound, alternative model for the time and mode of exhumation of the high-temperature metamorphic rocks of Unit IV is hampered by the total lack of thermo-chronological data in the area. D3 thrusting and erosion certainly contributed to exhumation of the metamorphic rocks, but the close spatial association of different metamorphic facies within one and the same D3 tectonic unit indicates that large part of the exhumation occurred previous to D3, but after D2. This is consistent with the unconformities of the Cretaceous on the Paleozoic (Early Cretaceous on late Permian, and Late Jurassic/ Early Cretaceous on early Paleozoic) that were mapped in the 1:100,000 Gole Gohar sheet of the Geological Survey of Iran. Thus exhumation of the syn-D2 metamorphic basement was largely a pre-D3 event, only amplified during D3 shortening and erosion.

## Barrovian metamorphism in the SSZ and comparison to other Cimmerian blocks

The peak P–T conditions described above (Fig. 12) correspond to mineral assemblages forming a pre-S2 fabric. The peak temperature conditions estimated by our thermodynamic modelling is ~ 20 °C lower than that estimated by the average P–T method (sample 71a: $674 \pm 24$ °C, $8.8 \pm 0.9$ kbar, sample 150: $691 \pm 42$ °C, $7.9 \pm 1.5$ kbar) for sample 71a and ~ 40 °C lower for sample 150. Peak pressure concord for both approaches, providing values of ca. 8–9 kbar. While thermodynamic modelling mostly allows to track the prograde path, it also suggests the existence of a clockwise P–T path accompanying incipient retrogression (Fig. 12).

P–T conditions estimated here confirm the occurrence of Barrovian metamorphism across the southern SSZ. The peak pressure estimated with our pseudosections (8.5–9 kbar; Fig. 12) matches previous estimates based on conventional thermobarometry (i.e. Sheikholeslami 2002; unpublished data $9.5 \pm 1.2$ kbar; Fazlnia et al. 2007; ~ 10 kbar). Previous peak temperature estimates ~ 700 °C (Sheikholeslami 2002; Fazlnia et al. 2007) are nevertheless higher than those assessed in the present study (~ 650 °C). Varying P–T estimates can result from different thermometric approaches and samples' difference.

Comparison of metamorphic data along strike of the SSZ shows that the pressure conditions of ~ 8–9 kbar, estimated by our work and previous literature are higher than those assessed in the northern SSZ (~ 4–6 kbar; see Sect. 2.3 and Fig. 14a; e.g. Baharifar 2009; Saki et al. 2011; Monfaredi 2015). Comparable metamorphic conditions have been reported (Fig. 14a) for the Mid-Cimmerian Shotur Kuh amphibolites (northern Central Iran; $P_{max}$: ~ 8 kbar, $T_{max}$: ~ 650 °C; Rahmati Ilkhchi et al. 2011), and the late Carboniferous (> ~ 320 Ma) amphibolite facies amphibolite-metagabbro unit, near Dorud (T: $700 \pm 20$ °C, P: $7.5 \pm 0.7$ kbar; Shakerardakani et al. 2016).

## Possible tectonic scenarios: Variscan or Eo-Cimmerian MP-HT metamorphism?

Correlating these new structural and petrological data allows us to propose new tectono-metamorphic evolutionary models of the southern SSZ. Structural data indicate the existence of two major fold generations. The F2 folds affected the pre-Triassic units, whereas the F3 folds affected all units, also including the Cretaceous (Kt, K1; UNIT I; Figs. 4a, 13). Microstructural relationships within Unit IV (Figs. c of online resource 2 and 8b) show that F2 and D2 took place under greenschist facies conditions, post-dating
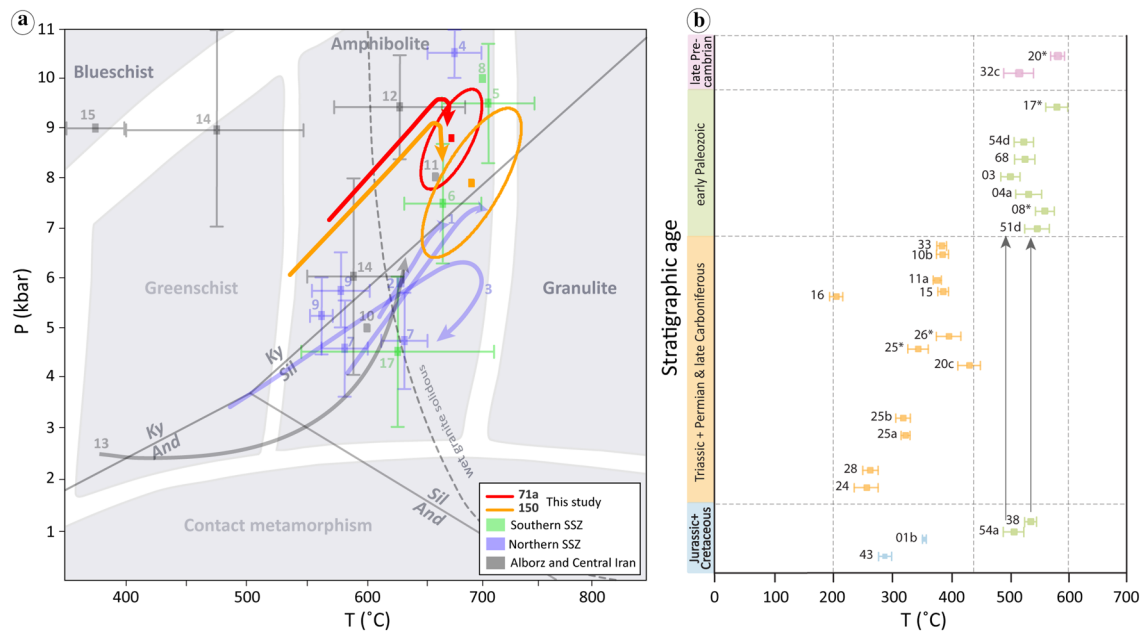


**Fig. 14** **a** Summary of P–T conditions and trajectories of regional metamorphism across the SSZ and other Cimmerian blocks (own data and compiled previous studies). The aluminosilicate triple point is from Holdaway (1971). References: (1) Shakerardakani et al. (2016), (2) Baharifar (2009), (3) Saki et al. (2011), (4) Davoudian et al. (2007), (5) Fazlnia et al. (2007), (6) Fazlnia et al. (2009), (7) Monfaredi (2015), (8) Sheikholeslami (2002), (9) Omrani et al. (2008), (10) Moazzen et al. (2020), (11) Rahmati Ilkhchi et al. (2011), (12) Rossetti et al. (2014), (13) Tabatabaei Manesh et al. (2010), (14) Zanchetta et al. (2009), (15) Zanchi et al. (2014). **b** Temperatures obtained by Raman spectrometry of carbonaceous material from SSZ (Gharibnejad et al. 2020). Sample number is given next to each sample and shown in Fig. 3

the high-temperature, Barrovian metamorphism, which corresponds to a geothermal gradient of ~ 20–25 °C/km, hence consistent with crustal thickening during collision (e.g. Hubbard 1989), by analogy with classical collisional belts. This relative timing between F2 folding/S2 and HT metamorphism is consistent with the fact that estimates of maximum temperatures (Gharibnejad et al. 2020; Fig. 14b) of Unit IV reveal higher metamorphic conditions for the early Paleozoic units (pre-Devonian rocks) than for the

late Paleozoic and Mesozoic ones, and the age of D2 folds (F2); hence of S2 can be constrained to be post-late Permo-Triassic (Fig. 5a, b). In addition, since the Jurassic (in the definition of Gharibnejad et al. 2020) does not appear to be affected by F2 folds, D2 is inferred to be pre-Jurassic. Therefore, D2 must be an Eo-Cimmerian event. However, the fact that only the Precambrian to early Paleozoic rocks experienced high-grade metamorphism (Gharibnejad et al. 2020; Fig. 14b) and no unconformity between the late and early
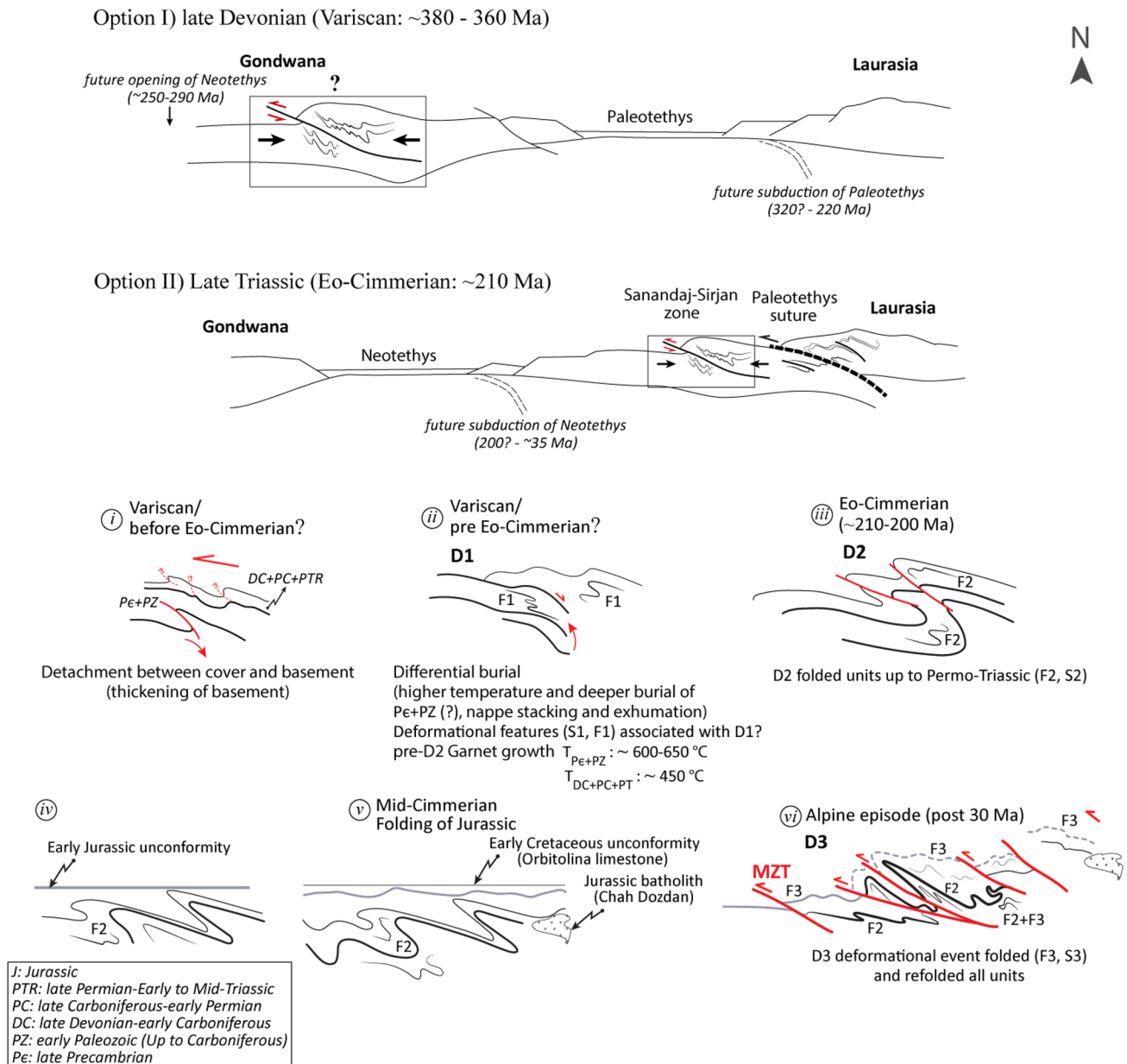


**Fig. 15** Geodynamic scenarios, suggesting two alternative evolution schemes to explain the first tectono-metamorphic phase observed in the SSZ and the following tectonic events. **a** Occurrence of high grade collision-related metamorphism in the northern edge of Gondwana. **b** Amphibolite grade metamorphism develops during the Eo-

Cimmerian episode following the closure of Paleotethys. Stages i–vi show the inferred structural and metamorphic evolution of the marked area in the SSZ. The north arrow aligns to the north direction of the present time.

Paleozoic or Precambrian has been documented, remains an open question in the geodynamic evolution of the SSZ. Indeed, no unconformity is explicitly shown nor mentioned yet in geological maps published by the Geological Survey of Iran (e.g. NW Qatruyeh map, 1:100,000; Sabzehei et al. 1999; and 1:100,000 geological map of Gole Gohar; Sabzehei et al. 1997a).

In order to explain this discrepancy, two alternative interpretations of the tectono-metamorphic evolution are proposed below, one with a first tectonic phase occurring during the Variscan (Fig. 15 option I) as opposed to one with a first tectonic phase of Eo-Cimmerian age (Fig. 15 option II).

(i) Variscan tectono-metamorphic event (D1)

This hypothesis requires that the onset of deformation and metamorphism took place at ~ 380–360 Ma in northern Gondwana (Fig. 15 option I). Assuming the first phase (D1) as Variscan, its inferred time range (Carboniferous), allows us to relate its metamorphism to the Paleotethyan rifting (~ 420 Ma: Stampfli and Borel 2002). One speculative option could be to envision the metamorphism resulting from the inversion of a small aborted rift formed during Paleotethys opening, possibly in response to far-field stresses associated with the onset of the subduction of the Paleotethys beneath Eurasia (Fig. 15 option I). Given the minimum age of ~ 350–300 Ma for eclogite facies metamorphism and ophiolitic complex in NW Alborz block (Zanchetta et al. 2009; Rossetti et al. 2017) and the Carboniferous age of the Anarak metamorphic complex (~ 333–320 Ma; Bagheri and Stampfli 2008; sequences metamorphosed under greenschist to amphibolite facies conditions and located in the southern active margin of Eurasia), subduction should have started before and possibly as early as ~ 360 Ma. A non-depositional surface of ~ 70 Ma separating late Devonian (Zakeen formation) and early Permian in the Zagros mountains (Ghavidel Syooki 2003; Fig. 2a) and geochronologic data from Neyriz (Watters et al. 1970; ~ 400 and 360 Ma) and Hajiabad (Ghasemi et al. 2002; ~ 330–301 Ma) regions would support the existence of Variscan metamorphism. Sheikholeslami et al. (2003, 2008) obtained Carboniferous $^{40}K$–$^{40}Ar$ metamorphic ages in the areas of Kuhe Sorkh ($310.3 \pm 9.1$ Ma) and Kore Sefid ($331.4 \pm 5.3$ Ma), in the southern SSZ, although they attributed the southern SSZ metamorphism of the Neyriz area to the Cimmerian orogeny.

(ii) Eo-Cimmerian tectono-metamorphic event (D1 + D2)

In this scenario, both the S1 and S2 schistosities and their associated D1 and D2 tectonic events, the second of which affected the stratigraphic sequence up to Permo-Triassic units (PTRd layers of UNIT IV; Figs. 4b, 13), would result from the Eo-Cimmerian episode associated with Paleotethys closure and subsequent collision (Fig. 15 option II). The Gole Gohar geological map (Geological Survey of Iran; Sabzehei et al. 1997a), which reports an unconformity between the Permo-Triassic (PTRd; Figs. 4b, 13) and the Triassic (TRbn; UNIT IV; Figs. 4b, 13) units, provides further support to attribute the peak P–T conditions and high temperature structural features (F1 and F2) to the Eo-Cimmerian phase. However, it is difficult to envision that a unique tectonic phase (Eo-Cimmerian) caused HT-MP metamorphism in some units (early Paleozoic rocks) and left the rest (late Paleozoic rocks; Carboniferous and Permian) under low-grade or even very low grade metamorphism, in spite of a rather homogeneous protolith (Pan-African basement). One solution would be to assume differential burial of the basement (Precambrian and early Paleozoic) and cover (here the Permian and Carboniferous units), for example through a major décollement (Fig. 15), to account for an abrupt increase of metamorphic grade with increasing stratigraphic age.

Following the first phase, which would include both F1 and F2 structures described above, the southern SSZ would be shortened in post-Cretaceous time (D3) under low temperature conditions that may be related to the Zagros orogeny. This folding and thrusting event, together with erosion, may be responsible for the final exhumation of the Barrovian metamorphic units. Along with this, thrusting of the SSZ onto the crush zone from the Oligocene onwards (Agard et al. 2005; Omrani 2008: ~ 25–28 Ma) may have given birth to units I–IV (Figs. 13, 15 option II). The parallelism of the F3 axial planes with the trend of the Zagros (NW–SE) suggests that this episode relates to the closure of the Neotethys, associated with minor crustal thickening (Paul et al. 2006, 2010), yet characterized by the lack of MP-HT metamorphism (Agard et al. 2011).

# Conclusion

Our new petrological investigations and structural analysis provide a better understanding of the tectono-metamorphic history and its geodynamic implications for the southern SSZ that we summarize below.

1. The southern SSZ can be described as the stack of four major tectonic units, parallel to the strike of the Zagros chain. The stacking of these units is inferred to be post-Cretaceous. The structurally highest unit (UNIT IV) is located in the eastern Gole Gohar region and consists of Precambrian and Paleozoic rocks at its base, followed by Mesozoic series. All of these units were thrust over

the Neyriz ophiolites, which form the footwall of the SSZ. Several phases of folding are recognized in the southern SSZ: a major phase of folding, which we term F2, manifested by tight to isoclinal folds is overprinted by open upright folds (F3). In addition, local evidence of an older folding event (F1) is present. The Precambrian and Paleozoic units (up to Permo-Triassic) contain similar (F2) and partly parallel (F3) folds, whereas the Mesozoic units (particularly the Cretaceous ones) were only affected by parallel folds (F3).

2. The structural grain of the SSZ results from the D2 and D3 tectonic events. D2, which is most likely of Eo-Cimmerian age, created a tightly folded structure and the dominant, regional schistosity, superimposed on a previous prograde metamorphic fabric. D3 refolded this structure and created a series of large thrusts, which accommodated post-Cretaceous shortening linked to the Zagros orogeny. Only circumstantial evidence exists for S1 and D1, but we speculate that S1 is associated to the high-grade, prograde metamorphism and that it is of pre-Cimmerian age, possibly Variscan. Burial and initial exhumation of the internal part of the SSZ may have already taken place during this phase.

3. Precambrian and early Paleozoic rocks of the southern SSZ experienced HT-MP amphibolite facies metamorphic conditions, whereas the younger units, including late Paleozoic (Carboniferous and Permian) and Mesozoic are poorly to non-metamorphosed. P–T results of the pseudosections in the pelitic MnNCKFMASHT system allow us to constrain the prograde metamorphic path of garnet-kyanite-bearing samples up to nearly upper amphibolite facies. Thermodynamic modelling indicates a clockwise P–T path with a geothermal gradient of ~20 °C/km and metamorphic peak at ~650 °C and 8–9 kbar. The peak conditions are followed by a slight decrease in temperature during decompression, probably related to the first phase of exhumation of the southern SSZ units.

## Declarations

## References

Agard P, Omrani J, Jolivet L, Mouthereau F (2005) Convergence history across Zagros (Iran): constraints from collisional and earlier deformation. Int J Earth Sci 94:401–419. https://doi.org/10.1007/s00531-005-0481-4

Agard P, Monié P, Gerber W, Omrani J, Molinaro M, Labrousse L, Vrielynck B, Jolivet L, Yamato P (2006) Transient, synobduction exhumation of Zagros blueschists inferred from P-T, deformation, time and kinematic constraints: implication for Neotethyan wedge dynamics. J Geophys Res. https://doi.org/10.1029/2005JB004103

Agard P, Omrani J, Jolivet L, Whitchurch H, Vrielynck B, Spakman W (2011) Zagros orogeny: a subduction-dominated process. Geol Mag 148:692–725

Aghanabati A (2013) Geological map of Abdoughi. Geological Survey of Iran, scale 1:250.000

Aghanabati A, Haghipour A (1975) Geological quadrangle map of tabas, sheet no. 1. Geological Survey of Iran, scale 1:250.000

Aghanabati A, Ruttner A, Nabavi M, Hajian J (1994a) Geological map of Shirgesht. Geological Survey of Iran, scale 1:100.000

Aghanabati A, Ruttner A, Nabavi M, Hajaian J, Alavi Naieni M (1994b) Geological map of Eshskabad. Geological Survey of Iran, scale 1:100.000

Alavi M (1996) Tectonostratigraphic synthesis and structural style of the Alborz mountain system in Northern Iran. J Geodyn 21(1):1–33. https://doi.org/10.1016/0264-3707(95)00009-7

Allen M, Ghassemi M, Shahrabi M, Qorashi M (2003) Accommodation of late Cenozoic oblique shortening in the Alborz range, northern Iran. J Struct Geol 25(5):659–672. https://doi.org/10.1016/S0191-8141(02)00064-0

Allen M, Kheirkhah M, Emami M, Jones S (2011) Right-lateral shear across Iran and kinematic change in the Arabia–Eurasia collision zone. Geophys J Int 184:555–574. https://doi.org/10.1111/j.1365-246X.2010.04874.x

Angiboust S, Agard P, Glodny J, Omrani J, Oncken O (2016) Zagros blueschists: episodic underplating and long-lived cooling of a subduction zone. Earth Planet Sci Lett 443:48–58

Azizi H, Stern R (2019) Jurassic igneous rocks of the central Sanandaj-Sirjan zone (Iran) mark a propagating continental rift, not a magmatic arc. Terra Nova 31(5):415–423

Bagheri S, Stampfli G (2008) The Anarak, Jandaq and Posht-e-Badam metamorphic complexes in central Iran: new geological data, relationships and tectonic implications. J Tectonophys 451:123–155

Baharifar A (Goldschmidt Conference Abstracts) (2009) PTt paths in dynamothermal metamorphic rocks of Hamadan area, Sanadaj-Sirjan. Geochimica et Cosmochimica Acta

Baharifar A, Moinevaziri H, Bellon H, Piqué A (2004) The crystalline complexes of Hamadan (Sanandaj-Sirjan zone, western Iran): metasedimentary Mesozoic sequences affected by Late Cretaceous tectono-metamorphic and plutonic events. CR Geosci 336:1443–1452

Baharifar A, Whitney D, Pang K, Chung S, Iizuka Y (2019) Petrology, geothermobarometry, and P-T path of spinel-bearing symplectite migmatites from the Simin area, Hamedan, Sansandaj-Sirjan Zone, Iran. Turk J Earth Sci. https://doi.org/10.3906/yer-1802-9

Ballato P, Nowaczyk N, Landgraf A, Strecker M, Friedrich A, Tabatabaei S (2008) Tectonic control on sedimentary facies pattern and sediment accumulation rates in the Miocene foreland basin of the southern Alborz mountains, northern Iran. Tectonics. https://doi.org/10.1029/2008TC002278

Barrier E, Vrielynck B, Brouillet J, Brunet M (2018) Paleotectonic reconstruction of the central tethyan realm. Tectonono-sedimentary-palinspastic maps from late permian to pliocene. Atlas of 20 maps (scale: 1:15.000.000). CCGM/CGMW, Paris. https://ccgm.org/en/

Berberian M (1983) Continental deformation in the Iranian plateau (contribution to the seismotectonics of Iran, part IV). Geoligal Survey of Iran, p 74

Berberian F, Berberian M (1981) In: Gupta H, Delany F (eds) Zagros Hindu Kush himalaya geodynamic evolution, vol 3. American Geophysical Union

Berberian M, King G (1981) Towards a paleogeography and tectonic evolution of Iran. J Earth Sci 8:210–265

Boulin J (1991) Structures in Southwest Asia and evolution of the eastern Tethys. Tectonophysics 196(3–4):211–268

Bourdelle F, Cathelineau M (2015) Low-temperature chlorite geothermometry: a graphical representation based on a T-$R^{+2}$-Si diagram. Eur J Mineral 27(5):617–626. https://doi.org/10.1127/ejm/2015/0027-2467

Bröcker M, Fotoohirad G, Abbaslu F, Rodionov N (2014) Geochronology of high-grade metamorphic rocks from the Anjul area, Lut block, eastern Iran. J Asian Earth Sci. https://doi.org/10.1016/j.jseaes.2013.12.021

Brunet M, Cloetingh S (2003) Integrated Peri-Tethyan Basins studies (Peri-Tethys Programme). Sed Geol 156(1–4):1–10. https://doi.org/10.1016/S0037-0738(02)00279-8

Buchs D, Bagheri S, Martin L, Hermann J, Arculus R (2013) Paleozoic to Triassic ocean opening and closure preserved in Central Iran: constraints from the geochemistry of meta-igneous rocks of the Anarak area. Lithos 172–173:267–287

Chiu H, Chung S-L, Zarrinkoub S, Mohammadi M, Khatib M, Iizuka, Y. Y (2013) Zircon U-Pb age constraints from Iran on the magmatic evolution related to Neotethyan subduction and Zagros orogeny. Lithos 162:70–87

Connolly J (2005) Computation of phase equilibria by linear programming: a tool for geodynamic modeling and its application to subduction zone decarbonation. Earth Planet Sci Lett. https://doi.org/10.1016/j.epsl.2005.04.033

Crawford A (1977) A summary of isotopic age data for Iran, Pakistan and India. Mem Soc Geol France 8:251–260

Davoudian A, Genser J, Dachs E, Shabanian N (2007) Petrology of eclogites from north of Shahrekord, Sanandaj-Sirjan Zone, Iran. J Mineral Petrol 92:393–413

Davoudian A, Genser J, Neubauer F, Shabanian N (2016) $^{40}Ar/^{39}Ar$ mineral ages of eclogites from North Shahrekord in the Sanandaj-Sirjan Zone, Iran: implications for the tectonic evolution of Zagros orogen. Gondwana Res 37:216–240

Delaloye M, Desmons J (1980) Ophiolites and mélange terranes in Iran: a geochronological study and its paleotectonic implications. Tectonophysics 68:83–111. https://doi.org/10.1016/0040-1951(80)90009-8

Dilek Y, Furnes H (2011) Ophiolite genesis and global tectonics: geochemical and tectonic fingerprinting of ancient ocean ic lithosphere. Geol Soc Am Bull 123(3–4):387–411. https://doi.org/10.1130/B30446.1

Dilek Y, Newcomb S (2003) Ophiolite concept and its evolution of geological thought. Geol Soc Am. https://doi.org/10.1130/0-8137-2373-6.1

Falcon N (1967) The geology of the northeast margin of the Arabian basement shield. Adv Sci 24:31–42

Fazlnia A, Moradian A, Rezaei K, Moazzen M, Alipour S (2007) Synchronous activity of anorthositic and S-type granitic magmas in the Chah-Dozd an batholith, Neyriz, Iran: evidence of zircon SHRIMP and monazite CHIME dating. J Sci Islam Repub Iran 18:221–237

Fazlnia A, Schenk V, StraatenMirmohammadi FM (2009) Petrology, geochemistry, and geochronology of trondhjemites from the Qori Complex, Neyriz. Iran Lithos 1(12):413–433

Fazlnia A, Schenk V, Appel P, Alizadee A (2013) Petrology, geochemistry, and geochronology of the Chah-Bazargan gabbroic intrusions in the south Sanandaj-Sirjan zone, Neyriz, Iran. Int J Earth Sci 102:1403–1426. https://doi.org/10.1007/s00531-013-0884-6

Fergusson C, Nutman A, Mohajjel M, Bennett V (2016) The Sanandaj-Sirjan Zone in the Neo-Tethyan suture, western Iran: Zircon U-Pb evidence of late Palaeozoic rifting of northern Gondwana and mid-Jurassic orogenesis. Gondwana Res 40:43–57

François T, Agard P, Bernet M, Meyer B, Chung S, Zarrinkoub M, Burov E, Monié P (2014) Cenozoic exhumation of the internal Zagros: first constraints from low-temperature thermochronology and implications for the build-up of the Iranian plateau. Lithos 206–207:100–112

Fursich F, Wilmsen M, Seyed Emami K, Cecca F, Majidifard R (2005) The upper Shemshak formation (Toarcian–Aalenian) of the Eastern Alborz (Iran): biota and palaeoenvironments during a transgressive–regressive cycle. Facies 51:365–384

Gharibnejad P, Agard P, Rosenberg C, Omrani J, Kananian A (2020) Fossil thermal structure of the southern Sanandaj-Sirjan zone (SW Iran): implications for regional-scale tectonics. J Asian Earth Sci. https://doi.org/10.1016/j.jseaes.2020.104488

Ghasemi H, Juteau T, Sabzehei M, Whitechurch H, Ricou L (2002) The mafic–ultramafic complex of Sikhoran (central Iran): a polygenetic ophiolite complex. CR Geosci 334:431–438

Ghavidel Syooki M (2003) Palynostratigraphy of Devonian sediments in the Zagros Basin, southern Iran. Rev Palaeobot Palynol 127:241–268

Golonka J (2004) Plate tectonic evolution of the southern margin of Eurasia in the mesozoic and cenozoic. Tectonophysics 381(1–4):235–273

Haghipour A, Aghanabati A (1989) Geological map of Iran, 2nd edn. Geological Survey of Iran, Tehran

Hassanzadeh J, Wernicke B (2016) The Neotethyan Sanandaj-Sirjan zone of Iran as an archetype for passive margin-arc transitions. Tectonics 35:586–621

Hassanzadeh J, Stockli D, Horton B, Axen G, Stockli L, Grove M, Schmitt A, Walker J (2008) U-Pb zircon geochronology of late Neoproterozoic-Early Cambrian granitoids in Iran: implications for paleogeography, magmatism and exhumation history of Iranian basement. Tectonophysics 451:71–96

Haynes S, Reynolds P (1980) Early development of Tethys and Jurassic ophiolite displacement. Nature 283:561–563

Heidari S, Daliran F, Paquette J, Gasque D (2015) Geology, timing, and genesis of the high sulfidati on Au (–Cu) deposit of Touzlar, NW Iran. Ore Geol Rev 65:460–486. https://doi.org/10.1016/j.oregeorev.2014.05.013

Henry D, Guidotti C, Thomson J (2005) The Ti-saturation surface for low to medium pressure metapelitic biotites: implications for geothermometry and Ti-substitution mechanisms. Am Miner 90:316–328. https://doi.org/10.2138/am.2005.1498

Holdaway M (1971) Stability of andalusite and the aluminum silicate phase diagram. Am J Sci 211:97–131

Holdaway M (2000) Application of new experimental and garnet margules data to the garnet-biotite geothermometer. Am Miner 85:881–892

Holdaway M (2001) Recalibration of the GASP geobarometer in light of recent garnet and plagioclase activity models and versions of the garnet-biotite geothermometer. Am Miner 86:1117–1129

Holland T, Powell R (1998) An internally consistent thermodynamic data set for phases of petrological interest (updated in 2004). J Metamorph Geol 16:309–343

Holland T, Powell R (2000) Calculation of phase relations involving haplogranitic melts using an internally consistent thermodynamic dataset. J Petrol 42:673–683

Holland T, Powell R (2011) An improved and extended internally consistent thermodynamic dataset for phases of petrological interest, involving a new equation of state for solids. Metamorph Geol. https://doi.org/10.1111/j.1525-1314.2010.00923.x

Holland T, Baker J, Powell R (1998) Mixing properties and activity-composition relationships of chlorites in the system $MgO$–$FeO$–$Al_2O_3$–$SiO_2$–$H_2O$. Eur J Mineral 10:395–406

Horton B, Hassanzadeh J, Stockli D, Axen G, Gillis R, Guest B, Amini A, Fakhri MD, Zamanzadeh SM, Grove M (2008) Detrital zircon provenance of Neoproterozoic to Cenozoic deposits in Iran: Implications for chronostratigraphy and collision tectonics. Tectonophysics 451(1–4):97–122. https://doi.org/10.1016/j.tecto.2007.11.063

Hosseini B, Gorbani M, Pourmoafi M, Ahmadi A (2012) Identi fication of two different phases of metamorphosed granitoid in Kuh-Sefid Tootak anticline based on U-Pb Age dating. Geosci J Iran 21:57–66

Hubbard M (1989) Thermobarometric constraints on the thermal history of the main central thrust zone and Tibetan Slab, eastern Nepal Himalaya. J Metamorph Petrol 7(1):19–30. https://doi.org/10.1111/j.1525-1314.1989.tb00572.x

Huckriede R, Kürsten M, Venzlaff H (1962) Zur Geologie des Gebietes zwischen Kerman und Sagand (Iran). Geologisches Jahrbuch der BGR Hannover, pp 1–197

Hunziker D, Burg J, Bouilhol P, Quadt A (2015) Jurassic rifting at the Eurasian Tethys margin: Geochemical and geochronological constraints from granitoids of North Makran, SE Iran. Tectonics 34(3):571–593

Jackson J, Priestly K, Allen M, Berberian M (2002) Active tectonics of the South Caspian Basin. Geophys J Int 148(2):214–245. https://doi.org/10.1046/j.1365-246X.2002.01588.x

Jamshidibadr M, Masoudi F, Collins A, Cox G (2010) Dating of Precambrian metasedimentary rocks and timing of their metamorphism in the Soursat metamorphic complex (NW IRAN): using LA-ICP-MS, U-Pb dating of zircon and monazite. J Sci Islam Repub Iran 21(4):311–319

Jamshidibadr M, Collins A, Masoudi F, Cox G, Mohajjel M (2013) The U-Pb age, geochemistry and tectonic significance of granitoids in the Soursat complex, Northwest Iran. Turk J Earth Sci 22:1–31

Kargaranbafghi F, Neubauer F, Genser J (2015) The tectonic evolution of western Central Iran seen through detrital white mica. Tectonophysics 651–652:138–151. https://doi.org/10.1016/j.tecto.2015.03.019

Khalatbari-Jafari M, Juteau T, Bellon H, Whitechurch H, Cotton J, Emami H (2003) New geological, geochronological and geochemical investigations on the Khoy ophiolites and related formations, NW Iran. J Asian Earth Sci 23:507–535

Lanari P, Wagner T, Vidal O (2014) A thermodynamic model for di-trioctahedral chlorite from experimental and natural data in the system $MgO$-$FeO$-$Al_2O_3$-$SiO_2$-$H_2O$: applications to P-T sections and geothermometry. Contrib Mineral Petrol. https://doi.org/10.1007/s00410-014-0968-8

Lifshin E, Gauvin R (2001) Minimizing errors in electron microprobe analysis. J Microsc Microanal 7(2):168–177

Masoodi M, Yassaghi A, Nogole Sadat A, Neubauer F, Bernroider M, Friedl G, Genser J, Houshmandzadeh A (2013) Cimmerian evolution of the Central Iranian basement: evidence from metamorphic units of the Kashmar-Kerman Tectonic Zone. Tectonophysics 588:189–208

Mattei M, Cifelli F, Muttoni G, Rashid H (2015) Post-Cimmerian (Jurassic–Cenozoic) paleogeography and vertical axis tectonic rotations of Central Iran and the Alborz Mountains. J Asian Earth Sci 102:92–101. https://doi.org/10.1016/j.jseaes.2014.09.038

McCall G (1997) The geotectonic history of the Makran and adjacent areas of southern Iran. J Asian Earth Sci 15:517–531

McCall G (2002) A summary of the geology of the Iranian Makran. Geol Soc Lond Spec Publ 195(1):147–204. https://doi.org/10.1144/GSL.SP.2002.195.01.10

McQuarrie N, Hinsbergen D (2013) Retrodeforming the Arabia-Eurasia collision zone: age of collision versus magnitude of continental subduction. J Geol 41(3):315–318

Moazzen M, Hajialioghli R, Möller A, Droop G, Oberhänsli R, Altenberger U, Jahangiri A (2013) Oligocene partial melting in the Takab metamorphic complex, NW Iran: evidence from in situ U-Pb geochronology. J Sci Islam Repub Iran 24(3):217–228

Moazzen M, Salimi Z, Rolland Y, Brocker M, Hajialioghli R (2020) Protolith nature and PT evolution of Variscan metamorphic rocks from the Allahyarlu complex, NW Iran. Geol Mag. https://doi.org/10.1017/S0016756820000102

Mohajjel M, Fergusson C (2014) Jurassic to Cenozoic tectonics of the Zagros Orogen in north western Iran. Int Geol Rev 56:263–287

Mohajjel M, Fergusson C, Sahandi M (2003) Cretaceous-Tertiary convergence and continental collision, Sanandaj-Sirjan Zone, western Iran. J Asian Earth Sci 21:397–412

Mohajjel M, Baharifar A, Moinevaziri H, Nozaem R (2006) Deformation history, micro-structure and P-T-t path in ALS bearing schists, southeast Hamadan, Sanandaj-Sirjan zone. Iran J Geol Soc Iran 1:11–19

Monfaredi B (2015) Quantitative determination of the prograde P-T path by garnet zonation pattern from the Buchan-type pelitic schists of the Hamadan crystalline basement, Sanandaj-Sirjan zone, western Iran. Geophysical Research Abstracts, vol 17, EGU2015-6240-1

Monfaredi B, Hauzenberger C, Neubauer F, Schulz B, Genser J, Shakerardakani F, Halama R (2020) Deciphering the Jurassic-Cretaceous evolution of the Hamadan metamorphic complex during Neotethys subduction, western Iran. Int J Earth Sci. https://doi.org/10.1007/s00531-020-01893-x

Monié P, Agard P (2009) Coeval blueschist exhumation along thousands kilometers: Implications for subduction channel processes. Geochem Geophys Geosyst (G3). https://doi.org/10.1029/2009GC002428

Moosavi E, Mohajjel M, Rashidnejad N (2014) Systematic changes in orientation of linear mylonitic fabrics: an example of strain partitioning during transpressional deformation in north Golpaygan, Sanandaj–Sirjan zone, Iran. J Asian Earth Sci 94:55–67. https://doi.org/10.1016/j.jseaes.2014.07.003

Moradi A, Shabanian N, Davoudian A, Azizi H, Santos J, Asahara Y (2020) Geochronology and petrogenesis of the Late Neoproterozoic granitic gneisses of Golpayegan metamorphic complex: a new respect for Cadomian crust in the Sanandaj-Sirjan zone, Iran. Int Geol Rev. https://doi.org/10.1080/00206814.2020.1821251

Moritz R, Ghazban F, Singer B (2006) Eocene gold ore formation at Muteh, Sanandaj-Sirjan Tectonic Zone, Western Iran: a result of late-stage extension and exhumation of metamorphic basement rocks within the Zagros Orogen. Econ Geol 101:1497–1524

Morley C, Kongwung B, Julapour A, Abdolghafourian M (2009) Structural development of a major late Cenozoic basin and transpressional belt in central Iran: the central basin in the Qom-Saveh area. Geosphere 5(4):325–362

Mouthereau F, Lacombe O, Vergés J (2012) Building the Zagros collisional orogen: timing, strain distribution and the dynamics of Arabia/Eurasia plate convergence. Tectonophysics 532–535:27–60

Newton R, Charlu T, Kleppa O (1980) Thermochemistry of the high structural state plagioclases. Geochim Cosmochim Acta 44:933–944

Nutman A, Mohajjel M, Bennett V, Fergusson C (2014) Gondwanan Eoarchean Neoproterozoic ancient crustal material in Iran and Turkey: zircon U Pb–Hf isotopic. Can J Earth Sci 51:272–285

Omrani J (2008) The geodynamic evolution of Zagros: tectonics and petrological constrains from the internal zone. Unpub. PhD. Universite de Paris 6

Omrani J, Agard P, Whitechurch H, Benoit M, Prouteau G, Jolivet L (2008) Arc-magmatism and subduction history beneath the Zagros Mountains, Iran: a new report of adakites and geodynamic consequences. Lithos 106:380–398

Omrani H, Moazzen M, Oberhänsli R, Tsujimori T, Bousquet R, Moayyed M (2013) Metamorphic history of glaucophane-paragonite-zoisite eclogites from the Shanderman area, northern Iran. J Metamorph Geol 31(8):791–812. https://doi.org/10.1111/jmg.12045

Paul A, Kavianian A, Hatzfeld D, Vergne J, Mokhtari M (2006) Seismological evidence for crustal-scale thrusting in the Zagros mountain belt (Iran). Geophys J Int 166(1):227–237. https://doi.org/10.1111/j.1365-246X.2006.02920.x

Paul A, Hatzfeld D, Kaviani A, Tatar M, Pequegnat C (2010) Seismic imaging of the lithospheric structure of the Zagros mountain belt (Iran), tectonic and stratigraphic evolution of Zagros and Makran during the mesozoic-cenozoic. J Geol Soc Lond Spec Publ 330:5–18. https://doi.org/10.1144/SP330.2

Rachidnejad-Omran N, Emami M, Sabzehei M, Rastad E, Bellon H, Piqué A (2002) Lithostratigraphie et histoire paléozoïque à paléocène des complexes métamorphiques de la région de Muteh, zone de Sanandaj-Sirjan (Iran méridional). Comp Rend L'acad Sci 334:1185–1191

Rahimi H, Moeinzadeh H, Moazzen M (2021) Geochemistry and geochronology of amphibolites from the Sirjan area, Sanandaj-Sirjan zone of Iran: Jurassic metamorphism prior to Arabia and Eurasia collision. J Geodyn. https://doi.org/10.1016/j.jog.2020.101786

Rahmati Ilkhchi M, Faryad S, Holub F, Kosler J, Frank W (2011) Magmatic and metamorphic evolution of the Shotur Kuh metamorphic complex (Central Iran). Int J Earth Sci 100:45–62. https://doi.org/10.1007/s00531-009-0499-0

Rahnati Ilkhchi M, Jeřábekac P, Faryada S, Koyid H (2010) Mid-Cimmerian, early alpine and late cenozoic orogenic events in the Shotur Kuh metamorphic complex, Great Kavir block, NE Iran. Tectonophysics 494(1–2):101–117. https://doi.org/10.1016/j.tecto.2010.09.005

Ramezani J, Tucker R (2003) The Saghand region, Central Iran: U-Pb geochronology, petrogenesis and implications for Gondwana tectonics. Am J Sci 303:622–665

Ricou L (1974) L'evolution geologique de la region de Neyriz (Zagros Iranien) et l'evolution structurale Zagrides. These d'etat, universite d'Orsay, France

Ricou L (1994) Tethys reconstructed: plates, continental fragments and their boundaries since 260 Ma from Central America to Southeastern Asia. Geodin Acta 7:169–218

Rossetti F, Nozaem R, Lucci F, Vignaroli G, Gerdes A, Nasrabadi M, Theye T (2014) Tectonic setting and geochronology of the Cadomian (Ediacaran-Cambrian) magmatism in Central Iran, Kuh-e-Sarhangi region (NW Lut Block). J Asian Earth Sci. https://doi.org/10.1016/j.jseaes.2014.07.034

Rossetti F, Monié P, Nasrabady M, Theye T, Lucci F, Saadat M (2017) Early Carboniferous subduction-zone metamorphism preserved within the Palaeo-Tethyan Rasht ophiolites (western Alborz, Iran). J Geol Soc. https://doi.org/10.1144/jgs2016-130

Sabzehei M, Eshraghi S, Rowshanravan J (1994a) Geological map of Zardu (Scale 1:100.000). Gological Survey of Iran, Tehran

Sabzehei M, Rowshanravan J, Eshraghi S (1994b) Geological map of Chahak (Scale 1:100.000). Geological Survey of Iran, Tehran

Sabzehei M, Rowshanravan J, Amini B (1995) Geological map of the Kor-e-Sefid area (scale 1:100.000). Geological Survey of Iran, Tehran

Sabzehei M, Eshraghi S, Rowshanravan J, Mahabadi S, Navazi M (1996) Geological map of Neyriz (Scale 1:100.000). Geological Survey of Iran, Tehran

Sabzehei M, Eshraghi S, Rowshanravan J, Gavidel M, Seraj M (1997a) Geological map of Gole Gohar. Geological Survey of Iran, Tehran

Sabzehei M, Rowshanravan J, Eshraghi S, Navazi M (1997b) Geological map of Sirjan, scale 1:100.000. Geological Survey of Iran, Tehran

Sabzehei M, Eshraghi A, Roshanravan J, Navazi M, Hamdi M, Ghavidel M (1999) Geological map of the Qatruyeh area (scale 1:100.000). Geological Survey of Iran, Tehran

Safarzadeh E, Masoudi F, Hassanzadeh J, Pourmoafi SM (2016) The presence of Precambrian basement in Gole Gohar of Sirjan (south of Iran). J Petrol (Persian) 26:153–170

Saki A, Moazzen M, Oberhansli R (2011) P-T evolution of the Precambrian Metamorphic Complex, NW Iran: a study of metapelitic rocks. Geol J 46:10–25

Sarkarinejad K (2007) Quantitative finite strain and kinematic flow analyses along the Zagros transpression zone, Iran. Tectonophysics. https://doi.org/10.1016/j.tecto.2007.04.007

Sarkarinejad K, Azizi A (2008) Slip partitioning and inclined dextral transpression along the Zagros Thrust System, Iran. J Struct Geol 30:116–136

Sarkarinejad K, Keshavarz S (2010) Quantitative kinematic flow and strain analyses of the drag folds associated to the Sananadaj-Sirjan HP-LT metamorphic belt, southwestern Iran. In: The first international applied geological congress, Department of Geology, Islamic Azad University-Mashad Branch, Mashad, Iran, 26–28 April

Sarkarinejad K, Godin L, Faghih A (2009) Kinematic vorticity flow analysis and $^{40}Ar/^{39}Ar$ geochronology related to inclined extrusion of the HP–LT metamorphic rocks along the Zagros accretionary prism, Iran. J Struct Geol 31:691–709

Şengör A (1979) Mid-Mesozoic closure of Permo-Triassic Tethys and its implications. Nature 279(5714):590–593

Şengör A (1984) The Cimmeride orogenic system and the tectonics of Euraisa. Geological Society of America, 195.

Şengör A (1987) Tectonics of the Tethysides: orogenic collage development in a collisional setting. Annu Rev Earth Planet Sci 15:213–244

Sepahi A, Whitey D, Baharifar A (2004) Petrogenesis of Andalusite-Kyanite-Silimanite veins and host rocks, Sanandaj-Sirjanmetamorphic belt, Hamedan, Iran. Metamorp Geol 22(2):119–134

Sepahi A, Borzoei K, Salami S (2013) Mineral chemistry and thermobarometry of plutonic, metamorphic and anatectic rocks

from the Tueyserkan area (Hamedan, Iran). Geol Quart. https://doi.org/10.7306/gq.1108

Sepahi A, Jafari S, Osanai Y, Shahbazi H, Moazzen M (2018a) Age, petrologic significance and provenance analysis of the Hamedan low-pressure migmatites; Sanandaj-Sirjan Zone, west Iran. Int Geol Rev 33:1446–1461. https://doi.org/10.1080/00206814.2018.1517392

Sepahi A, Salami S, Lentz D, Mcfarlane C, Maanijou M (2018b) Petrography, geochemistry, and U-Pb geochronology of pegmatites and aplites associated with the Alvand intrusive complex in the Hamedan region, Sanandaj-Sirjan zone, Zagros orogen (Iran). Int J Earth Sci 107(3):1059–1096. https://doi.org/10.1007/s00531-017-1515-4

Seyed Emami K (2003) Triassic in Iran. Facies 48(48):91–106. https://doi.org/10.1007/BF02667532

Shafaii Moghadam H, Stern R (2015) Ophiolites of Iran: keys to understanding the tectonic evolution of SW Asia: (I) paleozoic ophiolites. J Asian Earth Sci 91:19–38

Shafaii Moghadam H, Brocker M, Griffin W, Li X, Chen R, O'Reilly S (2016) Subduction, high-P metamorphism, and collision fingerprints in South Iran: constraints from zircon U-Pb and mica Rb-Sr geochronology. Geochem Geophys Geosyst. https://doi.org/10.1002/2016GC006585

Shahbazi H, Siebel W, Pourmoafee M, Ghorbani M, Sepahi A, Shang C, Vousoughi Abedini M (2010) Geochemistry and U-Pb zircon geochronology of the Alvand plutonic complex in Sanandaj-Sirjan Zone (Iran): new evidence for Jurassic magmatism. J Asian Earth Sci 39(6):668–683

Shakerardakani F, Neubauer F, Masoudi F, Mehrabi B, Liu X, Dong Y, Mohajjel M, Monfarei B, Friedl G (2015) Panafrican basement and Mesozoic gabbro in the Zagros orogenic belt in the Dorud-Azna region (NW Iran): laser-ablation ICP–MS zircon ages and geochemistry. Tectonophysics 146–171:647–648. https://doi.org/10.1016/j.tecto.2015.02.020

Shakerardakani F, Neubauer F, Genser J, Liu X, Dong Y, Monfaredi B, Benroider M, Finger F, Waitzinger M (2016) Revealing the significance and polyphase tectonothermal evolution of a major metamorphic unit in an orogen: the central Sanandaj-Sirjan zone, Zagros Mts., Iran. Geophysical Research Abstracts, EGU2016, p 1

Shakerardakani F, Neubauer F, Bernroider M, Quadt VA, Peytcheva I, Liu X, Genser J, Monfaredi B, Masoudi F (2017) Geochemical and isotopic evidence for Carboniferous rifting: mafic dykes in the central Sanandaj-Sirjan Zone (Dorud-Azna, west Iran). Geol Carpath 68(3):229–247. https://doi.org/10.1515/geoca-2017-0017

Shakerardakani F, Hua Li X, Ling X, Li J, Tang G, Liu Y, Monfaredi B (2019) Evidence for Archean crust in Iran provided by ca 27 Ga zircon xenocrysts within amphibolites from the Sanandaj-Sirjan zone, Zagros orogen. Precambrian Res. https://doi.org/10.1016/j.precamres.2019.105390

Sheikholeslami M (2002) Evolution structurale et metamorphique de la marge sud de la microplaque de l'Iran central: les complexes metamorphiques de la region de Neyriz (Zone de Sanandaj-Sirjan). These, universite de Brest, p 194

Sheikholeslami M (2015) Deformations of Palaeozoic and Mesozoic rocks in southern Sirjan, Sanandaj-Sirjan Zone, Iran. J Asian Earth Sci 106:130–149

Sheikholeslami M, Bellon H, Emami H, Sabzehei M, Pique A (2003) Nouvelles données structurales et datations $^{40}$K–$^{40}$Ar sur les roches métamorphiques de la région de Neyriz (zone de Sanandaj-Sirjan, Iran méridional). Leur intérêt dans le cadre du domaine néo-téthysien du Moyen-Orient. Comp Rend Geosci 335:981–991

Sheikholeslami M, Pique A, Mobayen M, Sabzehei M, Bellon H, Emami H (2008) Tectonometamorphic evolution of the Neyriz

metamorphic complex, Quri-Kor-e-Sefid area (Sanandaj-Sirjan Zone, SW Iran). J Asian Earth Sci 31:504–521

Shirdashtzadeh N, Torabi G, Meisel T, Harris C, Morishita T, Tamura A (2020) Origin of Lower Paleozoic S-type magmatism in a northern terrane of Gondwana (Central Iran): Geochemical and isotopic approach. Period Mineral. https://doi.org/10.2451/2020PM960

Soffel H, Davoudzadeh M, Rolf C, Schmidt S (1996) New palaeomagnetic data from Central Iran and a Triassic palaeoreconstruction. Geolog Rundsch 85:293–302

Stampfli G (2000) Tethyan oceans. Geol Soc Lond Spec Publ 173:1–23

Stampfli G, Borel G (2002) A plate tectonic model for the Paleozoic and Mesozoic constrained by dynamic plate boundaries and restored synthetic oceanic isochrons. Earth Planet Sci Lett 196:17–33

Stern R (2005) Evidence from ophiolites, blueschists, and ultra-high pressure metamorphic terranes that the modern episode of subduction tectonics began in Neoproterozoic time. Geology 33(7):557–560. https://doi.org/10.1130/G21365.1

Stöcklin J (1968) Structural history and tectonics of Iran: a review. Am Assoc Petrol Geol Bull 52:1229–1258

Stöcklin J (1974a) Possible ancient continental margins in Iran. Geology of continental margins. Springer Verlag, NewYork, pp 873–887

Stöcklin J (1974b) Northern Iran: Alborz mountains. In: Spencer A (ed) Mesozoic–cenozoic orogenic belts: data for orogenic studies. Special Publication of the Geological Society of London, pp 213–234

Stöcklin J, Nabavi M (1969) Geological map of Boshruyeh. Geological Survey of Iran, scale 1:250.000

Stockli D, Hassanzadeh J, Stockli L, Axen G (2004) Structural and geochronological evidence for oligo-miocene intra-arc low-angle detachmentfaulting in the Takab-Zanjan Area, NW Iran. Abstract, Programs Geological Society of America, p 36

Tabatabaei Manesh S, Sharifi M, Romanko A (2010) P-T Conditions of the Jandagh Metapelitic Schists, Northeastern Isfahan province, Iran. Petrology 18(3):308–317. https://doi.org/10.1134/S0869591110030069

Takin M (1972) Iranian geology and continental drift in the Middle East. Nature 235:147–150

Talebian M, Jackson J (2002) Offset on the main recent fault of NW Iran and implications or the late Cenozoic tectonics of the Arabia-Eurasia collision zone. J Geophys 150:422–439

Terry RD, Chilingar GV (1955) Summary of "concerning some additional aids in studying sedimentary formations," by M.S. Shvetsov. J Sediment Res 25(3):229–234

Thiele O, Alavi-Naieni M, Assefi R, Houshmandzadeh A, Seyed-Emami K, Zahedi M (1968) Explanatory text of the Golpaygan Quadrangle E7.1:250.000. Geological Survey of Iran, Tehran, p 24

Watters W, Sabzehei M, Alavi-Tehrani M, Etminan H, Majidi B (1970) Preliminary report on the geology and topography of the metamorphic and igneous rocks of central part of the Neyriz Quadrangle. Geological Survey of Iran (internal report), p 113

Wells A (1969) The Crush Zone of the Iranian Zagros Mountains and its implications. Geol Mag 106:385–394

Whitechurch H, Omrani J, Agard P, Humbert F, Montigny R, Jolivert L (2013) Evidence for Paleocene-Eocene evolution of the foot of the Eurasian margin (Kermanshah ophiolite, SW Iran) from back-arc to arc: implications for regional geodynamics and obduction. Lithos 182–183:11–32. https://doi.org/10.1016/j.lithos.2013.07.017

Whitney D, Evans B (2010) Abbreviations for names of rock-forming minerals. J Am Mineral 95:185–187

Zanchetta S, Zanchi A, Villa I, Poli S, Muttoni G (2009) The Shanderman eclogites: a Late Carboniferous high-pressure event in the

NW Talesh Mountains (NW Iran). Geol Soc Lond Spec Publ 312:57–78. https://doi.org/10.1144/SP312.4

Zanchi A, Zanchetta S, Garzanti E, Balini M, Berra F, Mattei M, Muttoni G (2009) The Cimmerian evolution of the Nakhlak-Anarak area Central Iran and its bearing for the reconstruction of the history of the Eurasian margin. Geol Soc Lond Spec Publ 312(1):261–286

Zanchi A, Malaspina N, Zanchetta S, Berra F, Benciolini L, Bergomi M, Cavallo A, Javadi HR, Kouhpeyma M (2014) The Cimmerian accretionary wedge of Anarak, Central Iran. J Asian Earth Sci 102:45–72